2018

Nondestructive evaluation of concrete bridge columns rehabilitiated with fiber reinforced polymers using digital tap hammer and infrared thermography

Andrew Scott Wheeler

Nondestructive Evaluation of Concrete Bridge Columns Rehabilitated With Fiber Reinforced Polymers Using Digital Tap Hammer and Infrared Thermography

Andrew Wheeler

Problem Report submitted to the
Benjamin M. Statler College of Engineering and Mineral Resources
at West Virginia University
in partial fulfillment of the requirements
for the degree of

Master of Science
in
Civil Engineering

Udaya B. Halabe, Ph.D., P.E., Chair
Hota V. S. GangaRao, Ph.D., P.E.
Hema J. Siriwardane, Ph.D., P.E.

Department of Civil and Environmental Engineering
Morgantown, West Virginia

2018

Keywords: Digital Tap Hammer; Infrared Thermography; Fiber Reinforced Polymer; FRP; Composites; Debonds; Delaminations; Bridge Rehabilitation

ABSTRACT

Nondestructive Evaluation of Concrete Bridge Columns Rehabilitated With Fiber Reinforced Polymers Using Digital Tap Hammer and Infrared Thermography

Andrew Wheeler

In 2017, the American Society of Civil Engineers (ASCE) gave bridges in the U.S. a C+ rating. Almost four out of every ten bridges are 50 years or older. In 2016, there were on average 188 million trips across a structural deficient bridge each day. With such a large number of bridges needing replaced or repaired, transportation officials are utilizing various bridge rehabilitation techniques to provide a cost effective solution to such a widespread problem. One rehabilitation technique involves the application of Fiber Reinforced Polymer (FRP) composite wraps to strengthen various bridge components. The initial and in-service, evaluation and acceptance of such FRP systems are crucial to their overall success and serviceability. Previously, several traditional methods such as visual inspection and coin tap testing of FRP composites were accepted as common practice for inspecting the quality of material and structural components. This type of evaluation was very subjective and dependent on the inspector's level of experience. More recently, nondestructive testing (NDT) techniques can identify internal or external defects without affecting the form, or function of a structure. Digital Tap Hammer testing and Infrared Thermography (IRT) are two commonly used NDT techniques for field evaluation of civil infrastructure, because these techniques are user friendly and highly mobile. This problem report reviews the recent advances on the applications of digital tap hammer testing and infrared thermography at identifying defects in various elements of infrastructure and FRP composite wraps applied to bridge columns in southern West Virginia. Additionally, this report includes information on process of repairing dilapidated reinforced concrete columns in preparation for the installation of a FRP system. All of this will serve as a demonstration of how crucial non-destructive evaluation (NDE) is to the success of FRP bridge rehabilitation. Furthermore, the conclusions indicate a need for NDE to ensure quality control of field rehabilitation projects.

ACKNOWLEDGEMENTS

I would like to express my heartfelt appreciation to my academic and research advisor, Dr. Udaya B. Halabe for his generous support and guidance during my tenure in the Master of Science in Civil Engineering (MSCE) degree program. I am extremely grateful to Dr. Halabe for all of his continuous encouragement and assistance, without which I would have never accomplished this research study. It has been my privilege to work under Dr. Halabe, who is extremely knowledgeable and experienced in the field of nondestructive testing.

I would like to express my thanks to Dr. Hota V.S. GangaRao and Dr. Hema J. Siriwardane, for serving as members of my Advisory and Examining Committee. I would also like to thank Dr. Hota V.S. GangaRao for allowing me to work through the Constructed Facilities Center (CFC) for my field studies.

I am also gratefully appreciative of the educational experience and financial support I received in the form of a teaching assistantship and tuition waivers from the Department of Civil and Environmental Engineering at West Virginia University during my MSCE degree program. I would also like to extend thanks to the West Virginia Division of Highways (WVDOH) for supporting my graduate research assistantship for the field testing portion of the work through the Constructed Facilities Center at West Virginia University.

In addition, I would like to extend the deepest appreciation to my family (Mr. Scott Wheeler and Mrs. Shawn Wheeler) for their love and support as I completed this study, and throughout my tenure in the MSCE degree program.

Table of Contents

LIST OF FIGURES

LIST OF TABLES

1. INTRODUCTION

1.1 BACKGROUND

Nondestructive testing (NDT) encompasses a variety of testing techniques that permit the examination of materials or fundamental infrastructure components without compromising their integrity. Implementation of nondestructive testing early on in the construction phase of a project, and throughout the structure's life span, can impact the preventative maintenance plan of a structure and ultimately increase its service life. Structures both new and old can benefit from NDT techniques. NDT can provide insight about the quality of materials and construction procedures of new structures while older structures can be assessed for integrity, and existing conditions or designs can either be monitored or identified. With the speed and accuracy of NDT methods, NDT offers a cost-effective solution to enhance the service life of a structure. Many nondestructive tests have the ability to provide information about discontinuities (such as cracks, voids, inclusions, delaminations), dimensions (thickness, depth, rebar spacing), physical and mechanical properties (reflectivity, conductivity, elastic modulus), stress and dynamic response (residual stress, crack growth, wear and tear) and signature analysis (image content, frequency spectrum, field configuration) (Meghana et. al. 2013). Nondestructive examination methods have evolved to include a multitude of optical and acoustical techniques. More commonly used methods include Visual and Optical Testing, Radiography, Magnetic Particle Testing, Liquid Penetrant Testing, Acoustic Emission Testing, Ultrasonic Testing, Electromagnetic Testing, Leak Testing, Infrared/Thermal Testing, and Remote Field Testing (www.ndt-ed.org). As their titles imply, many of the methods identify damage by measuring, light or sound intensity, temperature, displacements, as well as the strength of electromagnetic field. Each nondestructive inspection method has its own set of advantages and disadvantages. Selection of the correct method depends on the particular application and one must also take into consideration any field abnormalities that may inhibit or affect certain types of testing. Location, access issues, type of material, and structure geometry are some of the variables to be considered when selecting the appropriate testing technique. This problem report concentrates on the application of two nondestructive techniques,

specifically, digital tap hammer and infrared thermography, and how the techniques were utilized to evaluate the rehabilitation of reinforced concrete columns on a West Virginia Department of Highways (WVDOH) owned bridge.

The digital (electronic) tap hammer manufactured by WichiTech Industries, Inc. is a rapid damage detection device (RD^3). Originally created for the aerospace industry, the digital tap hammer has expanded its range of effectiveness to civil infrastructure inspection. Some benefits include low cost, hand held, automatic display reset, and light weight. The accelerometer in the tip of the hammer translates the force-time pulse at the head after each tap into a voltage pulse. A circuit known as the Programmable Array Logic Integrated Circuit (PAL IC) accepts the signal, then measures the pulse amplitude (Georgeson et al. 1996). The PAL IC then measures the pulse width and displays the data in numerical form on the screen. If the tap of the hammer is too hard or too light, then the hammer normalizes the tap and the hammer reads zero. The width of the force-time pulse correlates to the mechanical impedance of the structure being examined. A delamination in the Fiber Reinforced Polymer (FRP) composite, or a debond between the FRP wrap and the concrete, will ultimately reduce the local stiffness, and produce a wider force-time pulse. Therefore, deviation from nominal pulse width indicates the presence of a debond (Georgeson et al. 1996).

Another popular NDT technique is, Infrared Thermography (IRT), and is commonly used in a variety of civil infrastructure applications. IRT is a non-invasive testing method that utilizes the thermal energy emitted by an object to depict its surface temperature profile that can then be connected with subsurface conditions. Thermal imaging is a process in which thermal radiation, which is invisible to the naked eye, is translated into a visual image. To complete this translation, an infrared camera is implemented to generate visible images from invisible infrared radiation emitted by an object. There are essentially two types of infrared thermography, Passive thermography and Active thermography (Avdelidis et al. 2011). For materials and structures which naturally have different temperatures than the ambient temperatures, passive thermography, is employed. Passive thermography involves capturing thermal images using an infrared camera without any prior heating. With respect to active thermography, an external heating source is required to generate relative temperature difference. With this technique, the part of the structure

which has to be investigated is heated either naturally or artificially and the transient change in temperature is observed by recording surface temperature as a function of time using infrared cameras. Debonded areas have different thermal conductivity, heat capacity, and thermal diffusivity, consequently affecting the rate of heat flow through a structure, thereby resulting in surface temperature difference compared to defect-free areas.

Infrared cameras have the ability to capture the thermal image of the surface of an object whose temperature ranges between -20^0C and $+2000^0$C to an accuracy of $\pm 0.1^0$C at an ambient temperature of 30^0C. The use of infrared thermography is an effective nondestructive technique for identifying discontinuities such as cracks, voids, inclusions, debonds near the surface of concrete, masonry, and composite structures. This problem report discusses the application of infrared thermography field testing on concrete bridge columns.

Fiber Reinforced Polymer (FRP), a composite material manufactured from fibers and resin, has become prevalent in the rehabilitation of deteriorating civil infrastructure and has proven to be an efficient and economical construction technique for repairing dilapidated civil infrastructure. FRP composites provide many desirable properties such as high strength and stiffness, light weight, durability, excellent corrosion resistance, impact and fatigue resistance, and low maintenance cost. This makes FRP composite an ideal material for wide applications in civil infrastructure (Liang et al. 2013). There are several types of FRP, however, glass and carbon fiber FRPs are most commonly used in civil infrastructure applications. The laminate structure provides the strength and stiffness while the epoxy, polyester, or nylon resin binds the fibers and act to transfer stresses between fibers. A deteriorated reinforced concrete beam, column, or other structural element can see their load carrying capacity increased by simply wrapping the member with FRP composite fabrics or by externally bonding FRP composite laminates. Problems during the installation process, such as high variances in ambient temperatures, inadequately bonded concrete, in service stresses, and incorrect mixing techniques can result in the development of debonds between the FRP and the underlying structural member. The formation of debonds results in reduction in strength and overall durability of the FRP bonded system. Improper bonding, or the lack thereof, can create complications within the FRP and concrete matrix that could potentially affect the overall performance rehabilitated member. Consequently, it is imperative that a quality

control program be established for detecting and analysing any debonds within the FRP/concrete matrix during rehabilitation process and throughout the service life of the structure. Nondestructive methods have an important role in identifying debonds, and simultaneously providing information about the debond dimensions and its severity. This problem report analyzes the rehabilitation of reinforced concrete columns, and the use of Glass Fiber Reinforced Polymer (GFRP) fabrics to enhance the rehabilitation. In addition to the literature review, this report also includes the field data collected from the WVDOH Turnpike Bridge project in Fayette County, West Virginia. The field data illustrates the usefulness of the IRT and the digital tap hammer for evaluating FRP applications in the field environment.

1.2 RESEARCH OBJECTIVES

The primary objectives of this research are:

(a) To conduct a literature review focusing on recent advances in digital tap hammer testing and infrared thermography applications for concrete, masonry, and reinforced concrete structures.

(b) To conduct a literature review focusing on application of various nondestructive techniques for FRP composite bonded structures.

(c) To explain the rehabilitation process of reinforced concrete bridge columns in the field on a West Virginia Department of Highways project.

(d) To demonstrate the usefulness of digital tap testing and infrared thermography testing in the field for detection of subsurface debonds in FRP composite wrapped concrete members during the rehabilitation process.

1.3 ORGANIZATION

This problem report is organized into six chapters. Chapter 1 presents the introduction, background information about digital tap hammer testing and infrared thermography along with objectives of this report. Chapter 2 focuses on the literature review regarding some of the recent studies and field applications of infrared thermography and tap hammer testing techniques in detecting subsurface debonds in concrete, masonry, and reinforced concrete structures. Chapter 3

describes the overall concrete column rehabilitation process. Chapter 4 illustrates and describes in detail the tap hammer and IRT equipment used to evaluate the FRP fabric wrap once installed on the columns. Chapter 4 also discusses the use of tap hammer and IRT testing in the field to examine the application of a glass fiber composite wrap to the newly repaired concrete columns. Chapter 5 presents the conclusions of this study and recommendations for future reinforced concrete rehabs involving FRP components. References cited within this problem report have been listed at the end of the report before the appendix section that contains detailed tables related to the results from field testing.

2. LITERATURE REVIEW INVOLVING THE USE OF NDT TECHNIQUES TO EVALUATE CONCRETE AND MASONRY STRUCTURES

2.1 DIGITAL TAP HAMMER TECHNIQUES

The subsequent sections discuss how digital tap hammers were derived from a demand in the NDT industry, and the applications of digital tap hammers in recognizing defects in composites and concrete members by means of reviewing previously published literature.

2.1.1 ELECTRONIC TAP HAMMER FOR COMPOSITE DAMAGAE ASSESSMENT

(Georgeson et al. 1996)

Introduction

Literature published by Georgeson et al. (1996) discusses how the creation of the tap hammer coined the "Rapid Damage Detection Device" (RD^3) was derived from the need to analyze and evaluate the increasing amounts of composites in the aerospace industry. The aircraft manufacturer Boeing sought to develop a low cost method for testing composite structures in an effort to replace the conventional coin tap inspection method. The coin tap method was a simple and effective method for examining sandwich structures, bonded joints and composite laminates, however, although the method was simplistic and cost effective, it did possess some drawbacks. This method was entirely dependent on the user's hearing and interpretation of results. It was also impossible to quantify data or results. This paper reveals Boeing's response to the issue that eventually lead to the development of a hand held RD^3device that would address the need for a cost effective NDT technique that would be able to measure local stiffness and produce quantitative results.

Description of the RD^3

Boeing's Commercial Airplane Group designed and built the first digital tap hammer prototype and was designated the Rapid Damage Detection Device (RD^3). The prototype consisted of a lightweight hammer with an internal accelerometer that was attached via a cable to the hand held control module. The control module contained digital logic components, liquid crystal display, and an automatic display reset, all within an impact resistant case. Durable rechargeable Nicad batteries allowed for 16 hours of continuous operation. Within the head of the hammer, was an accelerometer that translated the force-time pulse generated at the head after each tap into a voltage pulse. The pulse amplitude is then measured by the Programmable Array Logic Integrated Circuit (PAL IC). The pulse width at half-amplitude is then computed by the PAL IC which is then displayed on the LCD screen. There is a correlation between the force-time pulse and the mechanical impedance of the local structure that is in question. This phenomenon means that a wider force-time pulse is produced when a debond or delamination is present because defects tend to reduce the local stiffness of a composite. Thus, any deviation from nominal pulse widths indicates a deviation from the nominal/normal structure. Figures 2.1 and 2.2 represent the force-time pulse distributions over a "good' and "poor" region respectively. The pulse width remains quite constant across a relatively broad range of impacts. This means that various operators tapping at various levels will produce similar impact widths.

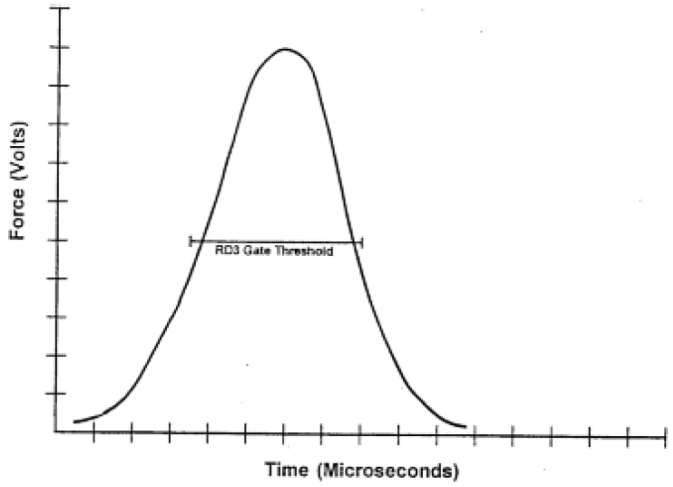

Figure 2.1: Typical RD^3 force-time pulse for a "good" region (Georgeson et al. 1996).

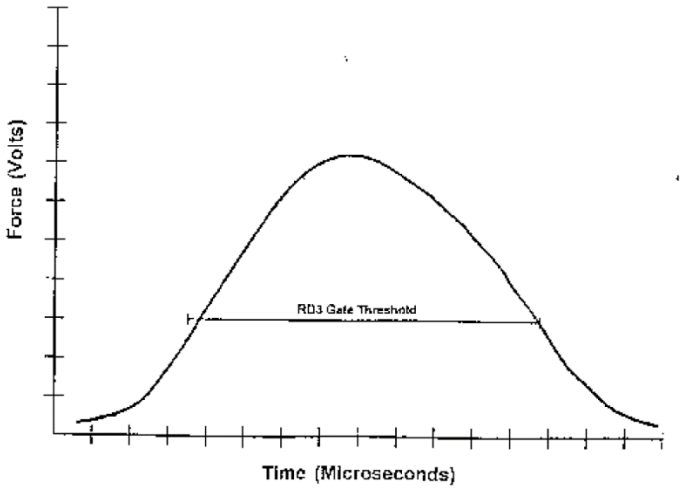

Figure 2.2: Typical RD^3 force-time pulse for a "poor" region (Georgeson et al. 1996).

Experimental Tests

For experimentation a sequence of nondestructive tests were executed on a specially designed sandwich step wedge. The step wedge was comprised of fiberglass/epoxy skins from one to seven plies thick that were bonded to a Nomex honeycomb core. Each skin was disbanded from the core which was representative of common defects found in sandwich panels. A single test consisted of an operator taking ten taps on a "good" region and ten taps and the "poor" disbanded region of each step. Results showed that there was a significant change in pulse widths for each thickness that were representative of disbanded areas. It was also found that as the thickness increased, the change in the pulse width created by the debond decreased. It is important to note that results indicated that a difference of 10% in pulse is easily discerned with the RD^3 where a difference of roughly 25% in pulse width is needed to be discerned by audible techniques. The RD^3 compared well another solenoid driven impact head bond tester used on the same step wedge. While the solenoid driven device provided slightly more sensitivity, the sensitivity was not a concern since the signals generated between bonded and debonded regions were so large. The RD^3 still performed well and was more cost efficient than the other options.

Additional tests on a damaged 747 Kreuger Flap verified that evaluating a composite via tap testing using the RD^3 could be accomplished using impact pulse width technology. These tests also proved that the RD^3could be used in a similar fashion as the traditional coin tap methods to locate defects, but did not require any special training to operate. The experiment showed that defects could be located and sized relatively quickly with no prior training or experience.

Conclusions

The creation and the evaluation of the RD^3 by Boeing filled a niche in the NDT market for a low cost hand held device that could be quickly implemented by inexperienced and experienced operators. Experiments conducted by the researchers have found that the RD^3 will work on sandwich panels up to 7 plies thick, and while the range of the device is dependent on the material and type of the structure, as well as type, size, and depth of the defect. Researchers were able to find that the RD^3 detected defects in 6 mm thick graphite/epoxy laminates. The RD^3 yielded similar results when compared to other higher priced instrumented tap hammers. RD^3 clearly has advantages over other methods such as user-friendly and low cost operation.

2.1.2 EVALUATION OF NON-DESTRUCTIVE INSPECTION METHODS FOR COMPOSITE AREOSPACE STRUCTURES

(Heida et al. 2011)

Introduction

Research conducted by Heida et al. (2011) was initiated by the Ministry of Defense in The Netherlands to investigate and develop procedures for the cost-effective inspection and repair of composite structures in the aerospace industry. Specifically, the aerospace industry began using an increasing amount of composite components in the manufacturing of military aircraft. A National Technology Program (NTP) was introduced to further study nondestructive inspections (NDI) on new and in service components. Researchers ultimately developed guidelines for NDI methods and the evaluation of NDI methods for composite aerospace structures.

Experimental Tests

A benchmark for the evaluation of NDI methods was established by first creating composite components designed for next generation aircraft. Components included solid laminates, sandwich structures, solid laminates with T-shaped stiffeners, and sandwich structures with L-shaped ribs and frames. The laminate configuration consisted of two different thicknesses: 2.7 and 5.4 mm. All of the composites were constructed of aerospace grade carbon fiber and HexPly M18-1 resin. Each of the specimens contained a number of real and artificial defects. Defects were dependent on panel configuration and were listed as:

- Range of impact damage with sizes relative to the BVID-value. Barley visible impact damage was herewith defined as impact damage with an initial dent depth of 1.0 mm.
- Interply delaminations in the (outer) skin with diameter in the range of 0.25 to 1.0 inch.
- Skin-to-stiffener disbands with diameter in the range of 0.25 to 2.0 inch.
- (Outer) skin-to-honeycomb core disbands with diameter in the range of 0.25 to 2.0 inch.

In order to compare a variety of NDI techniques, Heida et al. (2011) relied on ultrasonic C-scan inspection to create a base line of the defects present in each specimen. C-scan technology was considered to be the primary inspection technique for manufacturers of composites. C-scans are two-dimensional images produced by digitizing point-by-point signal variations of an interrogating sensor while it is scanned over a surface (Hsu et al. 2001). Figure 2.3 depicts the C-scan of a solid laminate with three T-shaped stiffeners with defects.

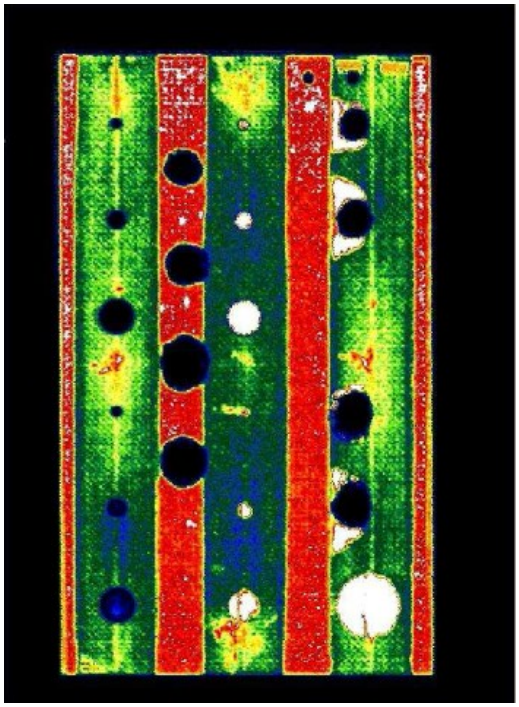

Figure 2.3: C-scan of solid laminate with defects (Heida et al. 2011).

Selection and Evaluation of NDI methods

NDI methods were selected based on how practical the method was for in-service use, proven applicability for the inspection of composite materials, and how cost effective the method was. One of the methods selected to be evaluated was automated tap testing. These tests were executed by nondestructive testing personnel within the Netherlands Defense Department using the Woodpecker WP-632. The Woodpecker WP-632, shown in Figure 2.4, is similar to the RD^3 device that was previously discussed in that it is hand held, however, the WP-632 implements a battery powered solenoid hammer with a built in force sensor, or accelerometer, in the head of the hammer. The Woodpecker measures the defects in the time that the head is in contact with the specimen. Areas with defects have a lower local stiffness, and thus the contact time will increase in those areas.

Figure 2.4: Woodpecker WP-632 by Mitsui Engineering & Shipbuilding Co (Heida et al. 2011).

Conclusions

The Woodpecker WP-632 is a cost efficient solution for smaller areas where defects are suspected. In applications where large areas need to be analyzed, the Woodpecker is less suitable because of its intermittent measurement style. While the WP-632 worked well in detecting impact damaged areas, the detection of debonds and delaminations were inconsistent. It was also found that a difference in skin thickness or the presence of a back-up structure affected the ability of the tap tester to detect debonds. The Woodpecker is limited in its ability to size defects, and this methodology is not suited for the estimating the depth of a defect. Overall, the study proved that a tap tester, such as the WP-632, would work well for detecting in-service composite structures that sustained impact damage. In the end, the strong capabilities of the WP-632 in detection of impact damage, portability, cost effective, and low levels of training, led researchers to ultimately recommend its use as an inspection device.

2.1.3 REMOTE RAILROAD BRIDGE STRUCTURAL TAP TESTING USING AERIAL ROBOTS

(Moreu et al. 2017)

Introduction

Rail systems throughout America account for transporting more than 40% of our nation's freight tonnage (Association of American Railroads 2014), thus maintaining the operational performance of our railroads is crucial to the American economy. North American railroad owners are faced with limited funding to address the increasing number of bridges in need of repair. Railroad bridge inspectors are interested in developing techniques that will efficiently quantify the structural condition of a bridge, and aide in prioritizing which bridges need to be replaced or repaired.

A large number of the bridges in need of repair are timber trestles. In most cases, these timber trestles have exceeded their expected life span. In an attempt to repair the bridges, the timber pier caps were replaced with concrete pier caps, however, an increase in train loading limits has brought the strength and serviceability of these new concrete pier caps into question. Railroad inspectors have made it a point to effectively assess the structural integrity of these concrete members, and attempt to determine what bridges require replacement or repairs first. Inspectors are implementing nondestructive testing techniques (NDT) to quantitatively asses the concrete elements in a quick manner, and inform bridge owners on the overall condition of the concrete members (Huston et al. 2011).

Researchers with Moreu et al. (2017) sought to investigate and possibly introduce new technology that would alleviate the costs associated with current tap testing methods. Modern tap testing inspections are costly and qualitative. Often times, inspections require the use of man lifts to permit access to the structure by inspectors. The research proposed the use of a remotely operated aerial tap testing device that would conduct tap testing on the structures in question, and collect impact sounds through a wireless sound system.

Equipment Development

Currently, there are no tap hammers capable of being used in conjunction with robots. Principles of this study decided to create a new tap hammer that was more suited for use in this particular application. Their design involved a closed loop and planar four-bar linkage, commonly referred to as a "crank-rocker". This design allows for the crank to rotate 360^0, and limits the rocker portion from 0^0 to 180^0. The entire device is powered by a six volt DC motor. In addition, the hammer is oriented upside down to prevent the hammer from coming into contact with the rotor blades of the drone. Figure 2.5 displays the concept behind the design. The mass and length of the hammer were configured so that the resonant frequency of the hammer would nearly match the rotational speed of the motor. This setup means that the motor and beam supporting the hammer remain in sync. Because each tap is mechanically controlled, the taps are produced with similar energies and frequency, thus human error is reduced.

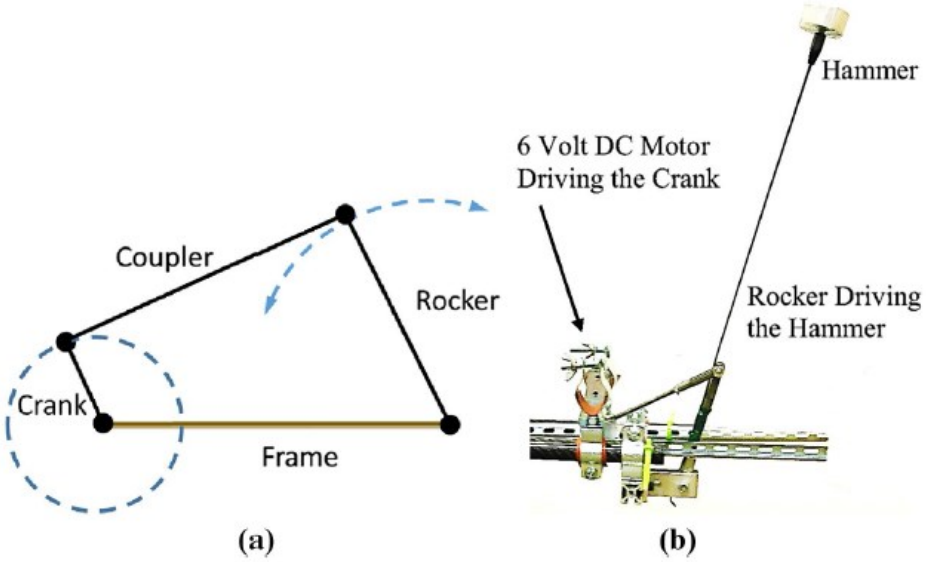

Figure 2.5: Aerial tap hammer mechanism consisting of a closed loop and planar four-bar linkage (Moreu et al. 2017).

Data acquisition was comprised of a TASCAMDR-44 digital recorder with four external microphones. Two microphones were installed on the body of the drone and two were placed in

close proximity to the tap hammer. These microphones could be controlled via a smartphone that connects to the digital recorder. Data would then be stored in an SD card that could be extracted post flight for data processing.

Experimental Tests

Experiments were divided into three groups: one test using a manually operated tap hammer, one to evaluate the automated tap tester, and measure the effect of noise created from the propulsion system on the microphones of the tap hammer. Initial testing involved using a manual operated tap hammer to evaluate two concrete specimens: a good concrete specimen and a bad concrete specimen. Figure 2.6 shows the key differences between the good and bad section. Note the bad section had holes drilled into the specimen as well as excessive corrosion induced by researches adding water to exposed rebar sections. This set of experiments would be used to create a baseline of performance for the automated tap hammer using the principal component analysis (PCA) to analyze results.

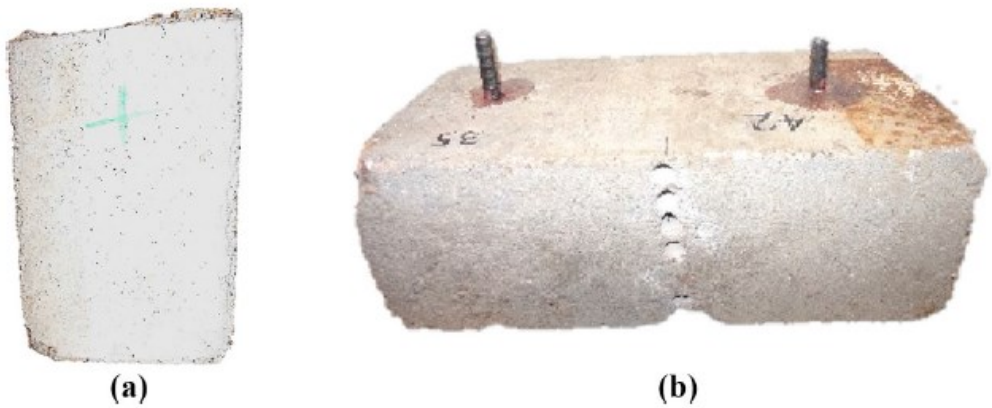

Figure 2.6: Test specimens used for characterizing manual tap testing where (a) represents good concrete and (b) represents bad concrete (Moreu et al. 2017).

Secondary experiments were the first to incorporate the use of the automated tap hammer. These experiments required that the tap hammer be fastened to the body of the drone where it would then be used to evaluate five specimens. The five specimens include concrete that was in

good condition as well as damaged concrete and with low compressive strength. The two additional specimens were comprised of plywood that varied in thickness from one to two sheets thick. This test was constructed to examine how the tap hammer performs with increased complexity in analyzing the results of all five specimens. Roughly 90 responses were collected per specimen per minute. The third experiment looked at how the remotely controlled device would interpret the acoustical results in the presence of the multirotor drone. During this set of tests nearly 150 responses were collected per specimen. For each experiment, PCA was used to generate clusters which were later classified based on structural properties. At this point a confusion matrix was generated to precisely quantify the classification performance. In essence this method of processing the data enables for the classification of different sounds and structures under scrutiny.

Conclusions

This research concluded that automated inspection of concrete elements is indeed feasible. Further developments include the creation and operation of a remote controlled acoustic impact response tap hammer. Members of the research team showed that hundreds of consistent impact response measurements could be collected relatively quickly from the structure. Evidence presented during the research supports the fact that differences between specimens can still be distinguished in the presence of a drone propulsion system. Although researchers did not complete flight testing, they establish parameters for the experimental phase of flight testing. Work also studies preliminary designs for mounting of the tap hammer to the drone. The implementation of this remote controlled tap hammer is not exclusive to drones. Supplementary uses include mounting of the device to remote controlled cars for use on numerous flat surfaces. Results have proven multiple uses of such technology not only in the railroad industry, but in any industry concerned with assessing infrastructure in a timely and cost effective manner.

2.2 INFRARED THERMOGRAPGHY TECHNIQUES

The following sections discuss how infrared thermography techniques (IRT) have complemented other NDT techniques, and the applications of infrared thermography in recognizing defects in bridge structures by means of reviewing previously published literature.

2.2.1 APPLICATION OF INFRARED THERMOGRAPHY TO THE NON-DESTRUCTIVE TESTING OF CONCRETE AND MASONRY BRIDGES

(Clark et al. 2003)

Introduction

The concept behind the study conducted by Clark et al. (2003) is based on the principle that many materials have the ability to absorb infrared radiation across a wide range of wavelengths. This phenomenon causes an increase the materials temperature. The thermal radiation pattern emitted by infrared energy is invisible to the human eye. Thermal imaging cameras are needed to convert the thermal radiation into a visual image. Infrared thermography has been applied to various professions that include the medical industry, firefighting, and even the printing industry (Clark et al. 2003). Civil engineers capitalized on this well known fact, and have implemented thermal imaging cameras into the field of nondestructive testing. While infrared thermography is widely used throughout civil engineering, the focus of this study was on the use of IRT to detect delaminations in bridges.

Testing and Outcomes

Analysis of a concrete bridge

A study was completed on a single span of a nine span masonry bridge on the M1 motorway in Northamptonshire in the UK. Because infrared thermography is susceptible to variances in temperature, the study was conducted over the course of two days in December of 2000 to see if the temperature on either day was more favorable than the other. Figure 2.7 shows the overall bridge with an arrow pointing to span 5 which was the primary span being studied. Span was selected due known delaminations being present. Infrared images were collected using an Agema Thermovision 900 Camera with a 20° lens. The entire device was connected to a laptop computer via an imaging software. The inspection was carried out at the ground level beneath the bridge. A digital camera was used to record visual images while the infrared camera was used to record temperature differences across the surface of the bridge along the span. Areas with temperature irregularities may indicate potential delaminations.

Figure 2.7: Photo of the bridge being studied with an arrow pointing to span 5 (Clark et al. 2003)

Infrared thermography proved to be so efficient that spans 1-5 as well as the south abutment were all scanned. Observations were made looking from west to east in span 5. Early on in the evaluation the camera was set to encompass all temperatures in the frame as shown in Figure 2.8. As testing progressed, camera settings were altered to exaggerate temperature variance. The settings were established as follows: distance from camera to object, 12 m, the atmospheric temperature was set at 11°C, and humidity set at 70%. Figure 2.9 illustrates two bands that are lighter in color due to those areas being warmer than surrounding areas as indicated by the two arrows. Figure 2.10 provides a clearer image of the delamination after an analysis tool was used to highlight the temperature band with a green color and the camera was moved closer to the object.

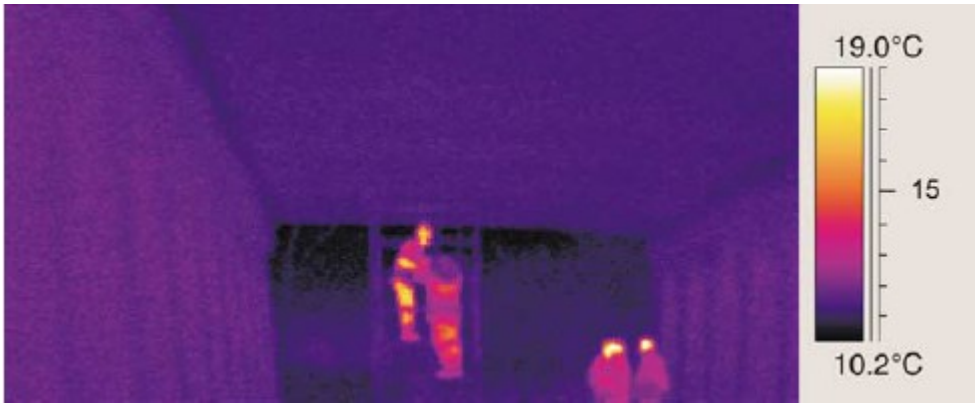

Figure 2.8: Infrared image looking down span 5 with all temperatures considered (Clark et al. 2003).

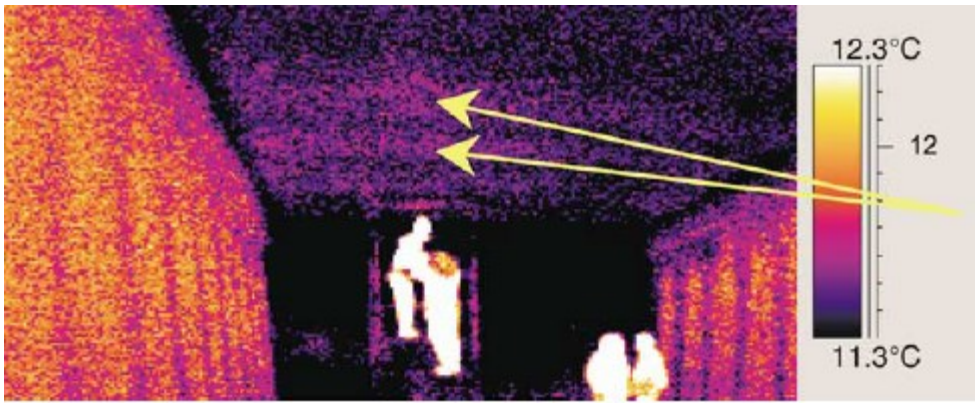

Figure: 2.9: Span 5 after camera setting were adjusted (Clark et al. 2003)

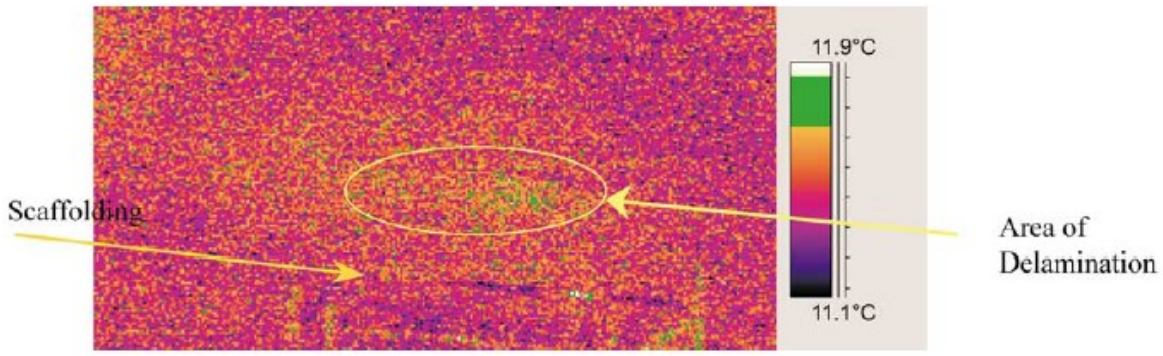

Figure 2.10: Span with the camera closer to object and after analysis tool was introduced (Clark et al. 2003).

Additional spans were studied and no obvious delaminations were found. These span included span 4, span 2 and span 1. Testing on span 3 did however suggest that delamination may be present. Figure 2.11 shows the infrared image with settings that create a different color scale to enhance the potential delamination. Analysis of the abutment was also performed, and while no delaminations were found, a damp area was noticed adjacent to a drain pipe. Table 2.1 provides a summary of the infrared study executed on the bridge.

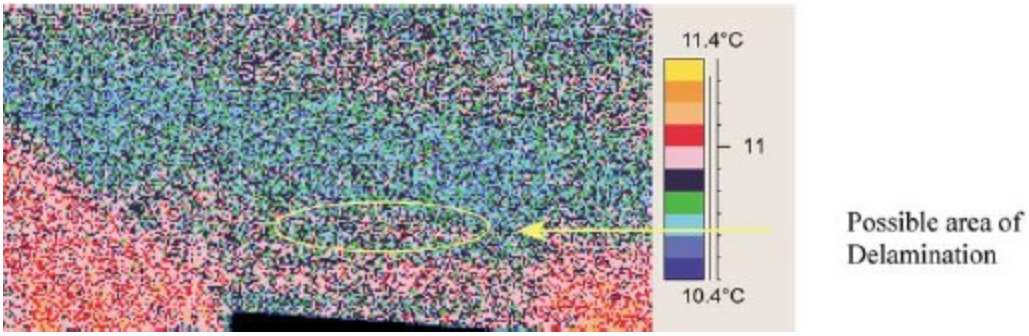

Figure 2.11: Possible delamination in span 3 (Clark et al 2003).

Table 2.1: Summary of results obtained from infrared thermography study (Clark et al. 2003).

Defect	Location	Previously identified by 'coin-tap test'
Delamination	West end of span 5	Yes
Delamination	East end of span 5 (3rd construction joint in)	No
Delamination	East end of span 5	Yes
Delamination	West end of span 3 (2nd construction joint in)	No
Delamination	West end of span 5 (near far end of span)	Yes
Delamination	East end of span 5 (near far end of span)	Yes
Delamination	West end of span 1 (near far end of span)	Yes
Damp patch	South abutment	Yes

Analysis of a masonry bridge

Similar investigations of the concrete bridge were performed on a smaller masonry bridge located at Kilbucho on the C road that links Broughton and Biggar on the north side of Goseland Hill. This particular bridge is a single span low rise skew brick arch with stone walls. The arch spans 3.6 m (11.81 feet) and the parapet walls reach a height of 1.1 m (3.60 feet). Figure 2.12 displays the bridge in its current setting. The bridge served as access to local farms, and the land surrounding the bridge is susceptible to localized flooding. The bridge can at times be submerged in the flood waters. Prior to the infrared study being conducted, the bridge was involved in an

accident where a vehicle hit the north end of the east side that resulted in several stones being knocked loose.

Figure 2.12: East side of the Kilbucho bridge (Clark et al. 2003).

Infrared analysis of the bridge took place in January of 2002 where the conditions were not ideal for such testing. Again, the Agema Thermovision 900 Camera with a 20 by 10^0 was used to perform the study. An image of the experimental setup can be seen in Figure 2.13. Unfortunately, due to in-situ conditions the entire bridge could not be viewed in a single infrared image. Researchers narrowed the temperature range so that only the objects of interest were shown. Preliminary infrared images included temperatures that allowed the surrounding plant and sky to interfere with the images. Analysis of the infrared images that were focused on the right side of the arch on the east side of the bridge indicated the possibility of water being behind the surface due to the arch being a darker color. Figure 2.14 shows the infrared image supporting this hypothesis.

Figure 2.13: Equipment setup of Kilbucho bridge (Clark et al. 2003)

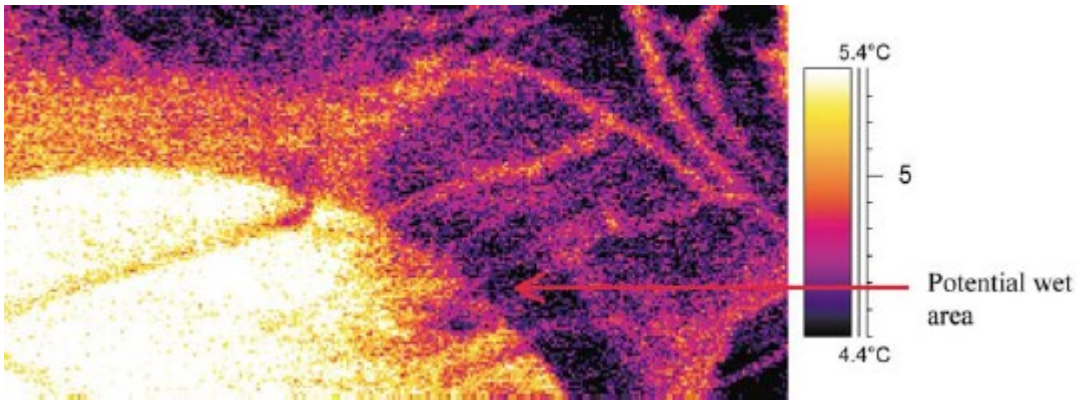

Figure 2.14: Infrared image on right side of arch on east side of bridge (Clark et al 2003).

The west side of the structure was examined following the east side. However, a large tree and steep slopes prevented clear infrared images from being produced. Because the bridge is essentially hidden between the embankments and behind the tree, any damp areas or potential delaminations will incorporate the entire bridge. Figure 2.15 and 2.16 show the visual representation and the infrared image from this vantage point respectively. Table 2.2 lists a summary of the results collected from the bridge.

Figure 2.15: West side visual of Kilbucho bridge (Clark et al. 2003).

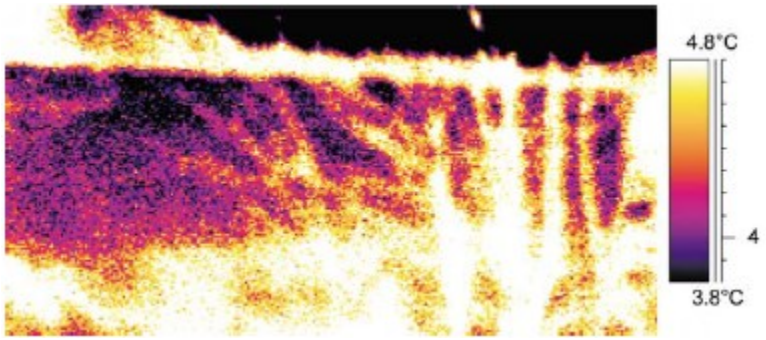

Figure 2.16: West side infrared of Kilbucho bridge (Clark et al. 2003).

Table 2.2: Summary of infrared study conducted on Kilbucho bridge (Clark et al. 2003).

Location of anomaly	Possible reason	Surface condition
South side of bridge on the left–hand side	Water in the fill	Dry
South side of bridge on the right–hand side	Water in the fill	Dry

Conclusions

The practice of using infrared thermography proved to be an efficient technique at identifying areas of delamination. Tests performed during these studies located two new delaminations that were previously undetected, and one of the new areas was tap tested and

confirmed as a delamination. In addition, all but one of the previously discovered delaminations were located via infrared thermography. The only area not confirmed by IR was near the exterior portion of the bridge and had been exposed to local sunshine. Temperature differences between the delaminated areas and non-delaminated areas was roughly 0.2-0.3^{0}C. While some of the tests performed during this study were efficient, it is important to consider the effects of the outdoors on the surface temperature of an object being studied. Weather conditions such as sunlight, rain, and wind can directly affect the temperature of an object, and because the radiation emitted by an object is a function of its temperature, the overall success of infrared thermography is dependent on the weather.

2.2.2 IR THERMOGRAPHY FOR THE INTERFACE ANALYSIS OF FRP LAMINATES EXTERNALLY BONDED TO RC BEAMS

(Valluzzi et al. 2008)

Introduction

The use of externally bonded fiber reinforced polymer (FRP) composites to reinforce and repair reinforced concrete (RC) beams are becoming more widespread. In most cases, the efficiency of this process is restricted by early brittle debonds forming between the surface and FRP. Thus, proper measures are required to monitor the initial set between the FRP and substrate to further prevent early delaminations. A combination of minor destructive (MD) and nondestructive (ND) methods are implemented to further evaluate and assess the quality of the bonds developed between the concrete and FRP. Minor destructive testing was comprised of pull-off and shear tests to study the overall quality of the bond. While there are a multitude of nondestructive techniques to choose from, each technique has their respective pros and cons, selecting the appropriate method depends on numerous parameters, such as environmental conditions, size and area of the defects, and accessibility to the areas selected for testing. Within the context of this study, infrared thermography was chosen for its high potential in assessing the effectiveness of strengthening structural members with FRP components. Full-scale experiments were executed on reinforced concrete beams to simulate a lack of bonding and air inclusions, and IRT was used to qualitatively detect the size and location of defects.

Experimental Tests

Small Specimen Testing

Initial tests were used to simply show that IRT has the ability to identify and locate defects prior to being used on the full-scale beams. For these tests, two square concrete slabs (40 x 40 x 5 cm) (15.748 x 15.748 x 1.968 in) were created using the same mix used for the large scale beams. Slabs were also cured under the same conditions as the full-scale beams. The first sample, it was expected that failure would occur at interface between the FRP and adhesive surface. In the case of the second sample, a thicker than normal layer of resin was applied to level the rough surface. Failure was expected to occur in the region where the thicker resin was present. Defects were simulated by using a variety of Teflon strips of dimensions 10 mm wide, 25 or 50 mm long, and roughly 30 um thick were placed on a side strip. Similar Teflon strips were placed in the middle strip of the specimens except these Teflon strips were 60 um thick and were double stacked. The last strip contained silicon grease approximately 80 um thick in areas that were 20 x 50, 20 x 30, and 20 x 20 mm. Also in the last strip were nylon squares that were either 25 x 25 or 10 x 10 mm wide and 100 um thick. Figure 2.17 shows the preparation of the specimens and the division of the strips. It is important to note that the defects were only placed on the rough side and were adhered to the surface via thin adhesive tape.

Figure 2.17: Preparation of specimens with simulated defects (a) smooth surface (b) rough surface (c) application of FRP (Valluzzi et al. 2008).

Examination of the specimens utilized the “active thermography” technique where the material was artificially heated using a pair of flash lamps. The lamps used produced 2,400 J of

energy in roughly 10 seconds. A FLIR ThermaCAM SC3000 with an image resolution of 240 x 320 FPA and a thermal resolution of 30 mK was used to take and collect the infrared images. The IR camera was placed a distance of 80 cm from the specimens. The camera collected temperature maps of the surface every 20 ms. Therefore, every preceding image collected by the device would be slightly warmer than the most recent or current image. Principal components analysis (PCA) was chosen for analysis to enhance defect detection capacity and to characterize the geometry in terms of depth. PCA was also favored because heating of the specimens is typically irregular and uneven, and PCA is not affected by these anomalies.

Full-scale Tests

Full-scale testing was performed on two reinforced concrete beams that were 10 m long and 30 x 50 cm. One beam contained normal reinforcement while the second one had additional prestressing steel. The underside of the beams were reinforced with pre-impregnated CFRP laminates with a tensile strength of approximately 2,800 MPa. The laminate was pretensioned during application by fixing one end and establishing a sliding anchor fixed to a hydraulic jack for pretensioning at the other end. Each beam was prepped and cleaned prior to the adhesion of the CFRP. A thin bed of resin used to smooth the surface and adhere the fibers of the laminate.

After the CFRP was applied, the beams were loaded to failure. The failure induced large-scale deformations that resulted in delaminations of the FRP fibers along the concrete substrate. IRT was employed prior to loading tests to evaluate any preliminary defects, and was continued throughout the loading period up till 67% of the failure load. A special cart was constructed to hold the thermocamera and a mirror at 45^0. The mirror reflected the image of the underside of the beam which was then captured by the camera. Figure 2.18 represents the device. This setup allowed for the device to be used in motion. Two IRT studies were performed on the beams. Qualitative scanning was performed once the beams were unloaded. For this test a heater was placed on the cart and spaced at a distance of 10 cm from the surface of the CFRP. The qualitative scanning was used to identify potential defects. Analysis of the results involved PCA techniques to further define the defects. The PCA analysis focused on two areas, the midspan and the anchorage zone.

Figure 2.18: IRT mobility cart (Valluzzi et al. 2008).

A second round of testing involved keeping the thermocamera stationary on suspected defects while applying heat manually for roughly 20 seconds at a distance of 5-10 cm. Again, PCA data was acquired prior to loading and three times during loading. Figure 2.19 displays the results from the beam with no prestressing steel at about one meter from mid-span. Figure 2.19a shows the PCA results after unloading has occurred. Figure 2.19b and c represent the PCA results at 27% and 67% of the failure load respectively. In both the unloaded and loaded state, one defect was identified. Similar results were found in the infrared and PCA analysis of beam containing prestressed steel. Figure 2.20 illustrates these results in the same fashion as Figure 2.19.

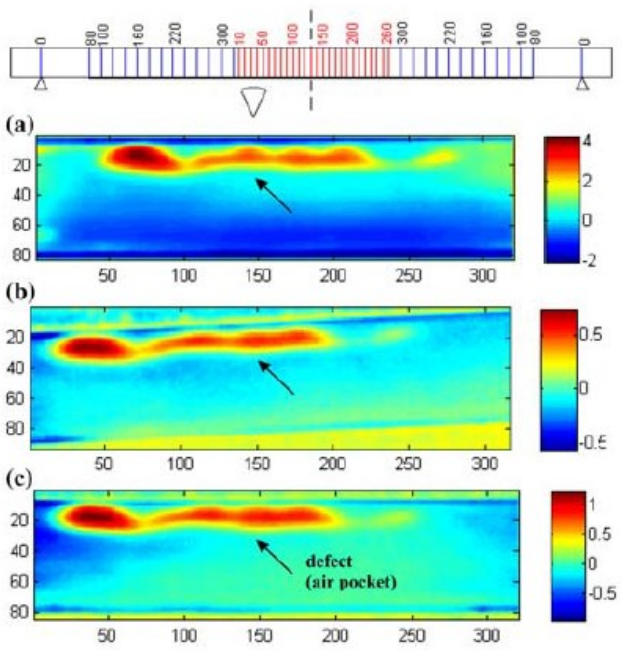

Figure 2.19: Infrared results from PCA analysis of the RC beam (Valluzzi et al. 2008).

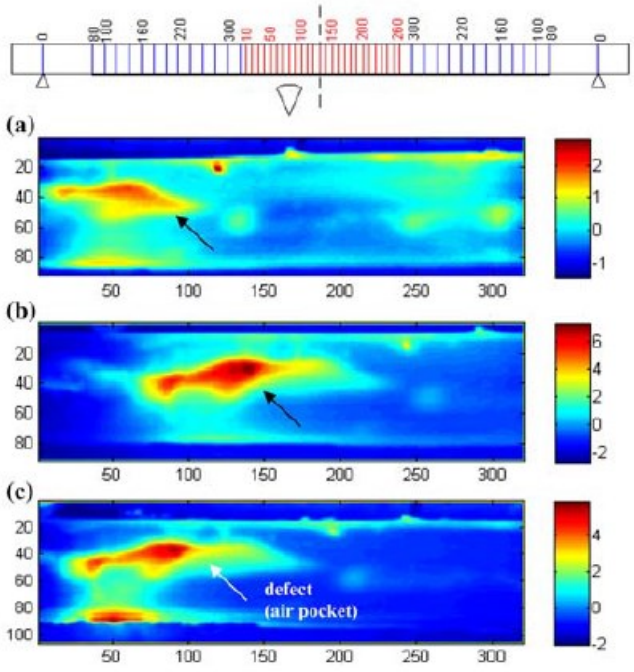

Figure 2.20: Infrared results from PCA analysis of the prestressed RC beam (Valluzzi et al. 2008).

Conclusions

Infrared analysis was applied as a nondestructive technique to identify subsurface defects at the interface of CFRP and reinforced concrete beams. Small-scale specimens were designed with intentional defects in the interface to characterize the parameters and to select the most appropriate method for analysis on the full-scale beams. Principal components analysis (PCA) was chosen since PCA is independent of how uniformly the heat is distributed across the beams. In the end, this method was able to locate defects in the interface between the FRP and concrete, and also provide a rough estimate of the defect's size. These results were confirmed by visual inspections after the beams had failed. Comparisons of the infrared results to the visual inspections after failure confirmed that infrared thermography is an effective nondestructive technique at identifying defects or potential defects in the FRP-substrate interface during and after loading.

2.2.3 NDE OF FRP WRAPPED COLUMNS USING INFRARED THERMOGRAPHY

(Halabe et al. 2008)

Introduction

A depleting infrastructure has led the construction industry to rehabilitate existing columns and structures with Carbon Fiber Reinforced Polymer (CFRP) and Glass Fiber Reinforced Polymers (GFRP) composites. Columns wrapped with Fiber Reinforced Polymer (FRP) composites see an increase in compressive strength, deformability and dynamic energy absorption. The FRPs used in such projects are comprised of a combination of either glass or carbon fibers and a matrix that is either an epoxy or a vinyl ester. FRP is an attractive alternative to other structural materials because of its lightweight, high strength, impact resistance, and corrosion resistive properties. Subsurface debonds between the FRP and column as well as delaminations can have a negative effect on the confinement delivered to the column by the FRP. This research study examined the effectiveness of infrared thermography (IRT) in detecting air-filled and water-filled debonds in FRP wrapped columns. In particular, this study investigated concrete cylinders wrapped in CFRP and GFRP composites with air-filled and water-filled debonds present between the FRP and concrete. Laboratory tests as well as field testing were performed to review the overall of effectiveness of IRT in this application.

Experimental Tests

Laboratory Testing

The laboratory component of this study involved the casting of twelve 6" x 12" concrete cylinders. Six of the cylinders were wrapped in GFRP and the remaining six cylinders were wrapped in CFRP. Resin used for bonding the FRP composites to the concrete substrate was manufactured by Fyfe Co. LLC. Air-filled and water-filled debonds were arranged in three size groups: 3" x 3", 2" x 2", and 1.4' x 1.4" all with a common thickness of 1/10". Air-filled debonds were constructed by cutting curved sheets to size from plastic containers that were the same size as the cylinders. Plastic spacers were also cut and glued to the plastic sheets to develop void areas or air pockets. Custom polyethylene pouches were utilized to contain water for the water-filled debonds. The artificial debonds were then glued to the cylinders prior to being wrapped with their respective FRP composite.

Infrared thermography testing was executed with a digital infrared camera produced by FLIR Systems. This particular camera was capable of detecting infrared radiation in the spectral range of 7.5 to 13 micron, and a thermal sensitivity of 0.06 ^{0}C at 30^{0}C. Images collected from the camera were stored on a connected laptop, and were later analyzed using a software provided by FLIR Systems. The surface temperature of the specimens were heated by means of two 1500W quartz tower heaters that were on rotating tables adjacent to the specimen. Figure 2.21 shows the laboratory testing setup. Test specimens were subjected to heat for 70 seconds after which the heaters were rotated away from the specimens. Even after the heat source was removed, the infrared camera continued to record information for several minutes so that the entire heating and cooling cycle was captured.

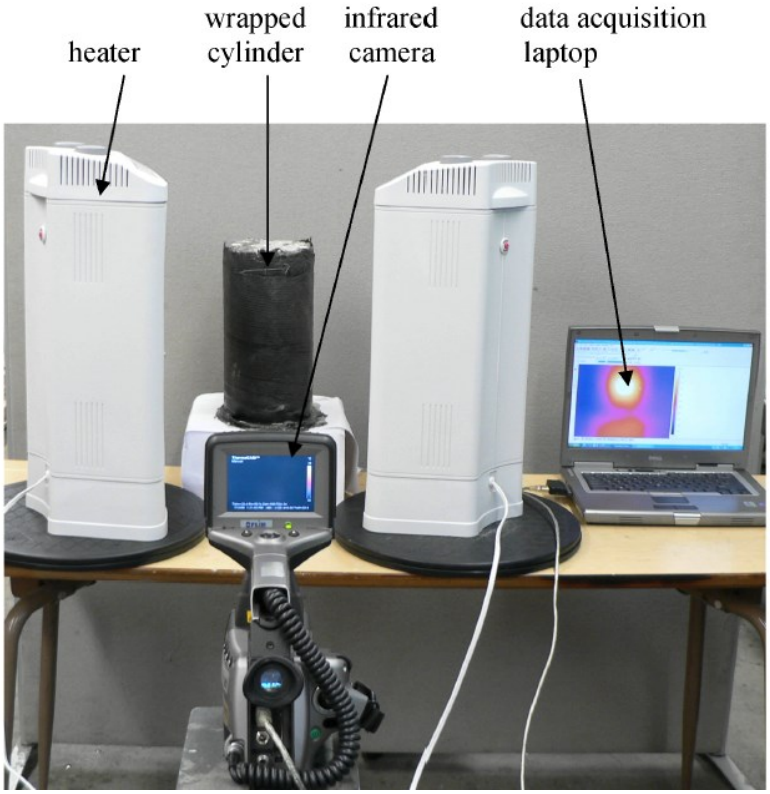

Figure 2.21: Laboratory equipment setup (Halabe et al. 2008).

Both air-filled and water-filled debonds in GFRP wrapped cylinders were successfully found using the infrared technology. All three sizes groups were displayed as "hot-spots" indicating that the surface temperature above the debond was higher than the surrounding debond-free areas. Figure 2.22 illustrates the "hot-spots" associated with the air-filled debonds in the infrared images of the GFRP wrapped columns. These "hot-spots" are due to the fact that defect-free regions conduct heat faster than regions with debonds. With respect to the water-filled debonds, they too were shown as "hot-spots" as seen in Figure 2.23. Typically, debonds containing water would not show up as hot spots because water conducts heat faster than defect-free regions. Thus, the surface temperature above the water-filled debonds would be lower than the regions above the defect-free areas. However, because these composite wraps were so thin, the heat was actually absorbed by the water due to water's high specific heat value. Therefore, the water-filled debonds appeared as "hot-spots".

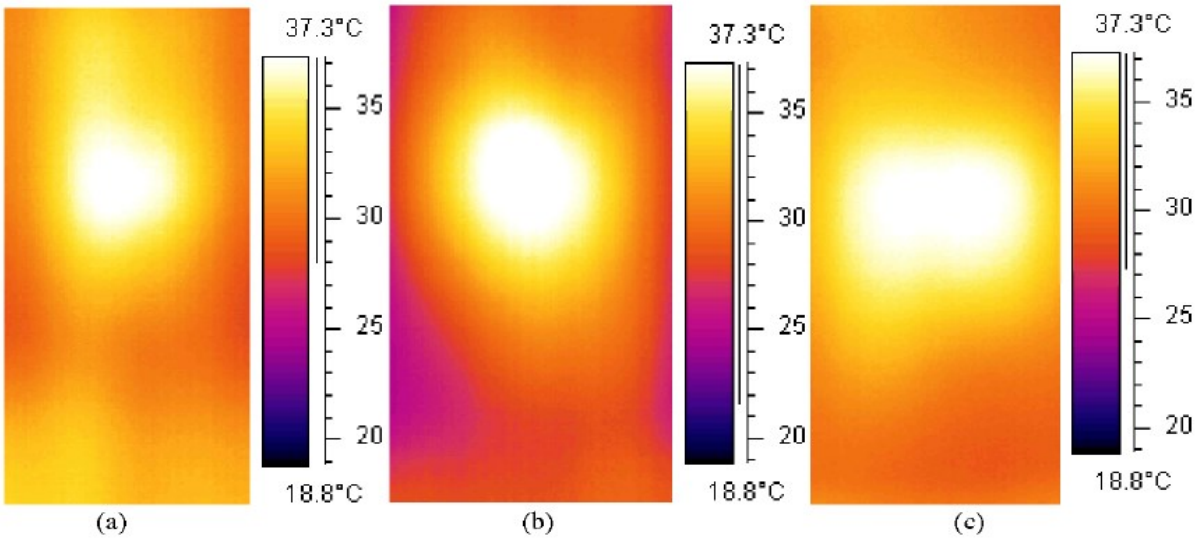

Figure 2.22: Air-filled debonds on GFRP wrapped cylinders (a) 1.4" x 1.4" specimen (b) 2" x 2" specimen (c) 3" x 3" specimen (Halabe et al. 2008).

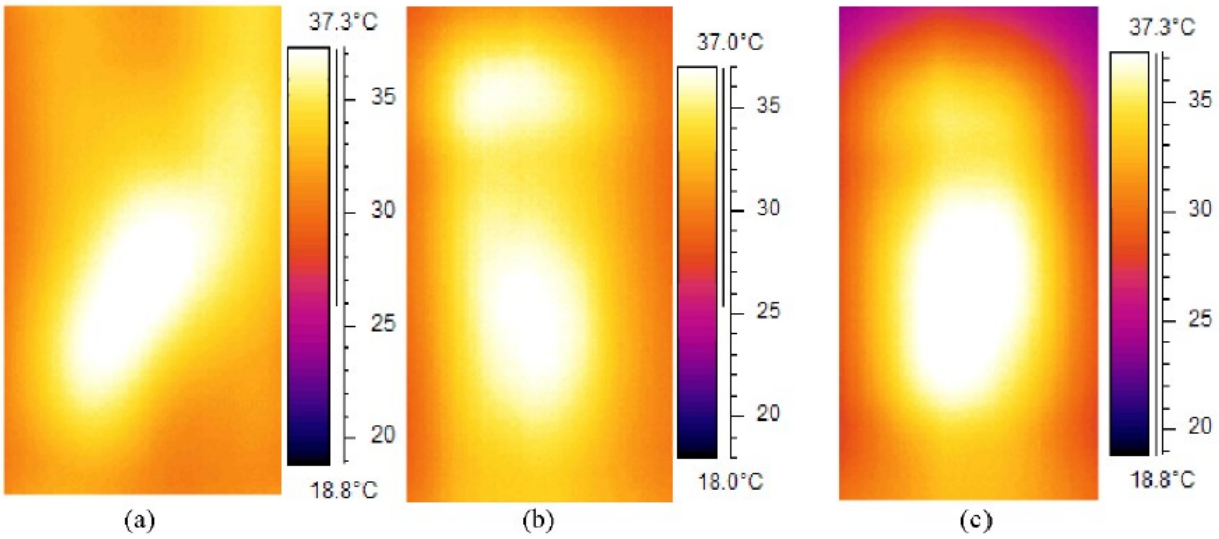

Figure 2.23: Water-filled debonds on GFRP wrapped cylinders (a) 1.4" x 1.4" specimen (b) 2" x 2" specimen (c) 3" x 3" specimen (Halabe et al. 2008).

Analysis of the CFRP wrapped cylinders produced similar results to the GFRP wrapped cylinders. Debonds were easily detected in both air-filled and water-filled samples. Explanations on why the results occurred this way were previously mentioned in the paragraph above. Figure

2.24 represents the infrared images accompanying the air-filled debonds while Figure 2.25 shows the infrared images of the water-filled debonds.

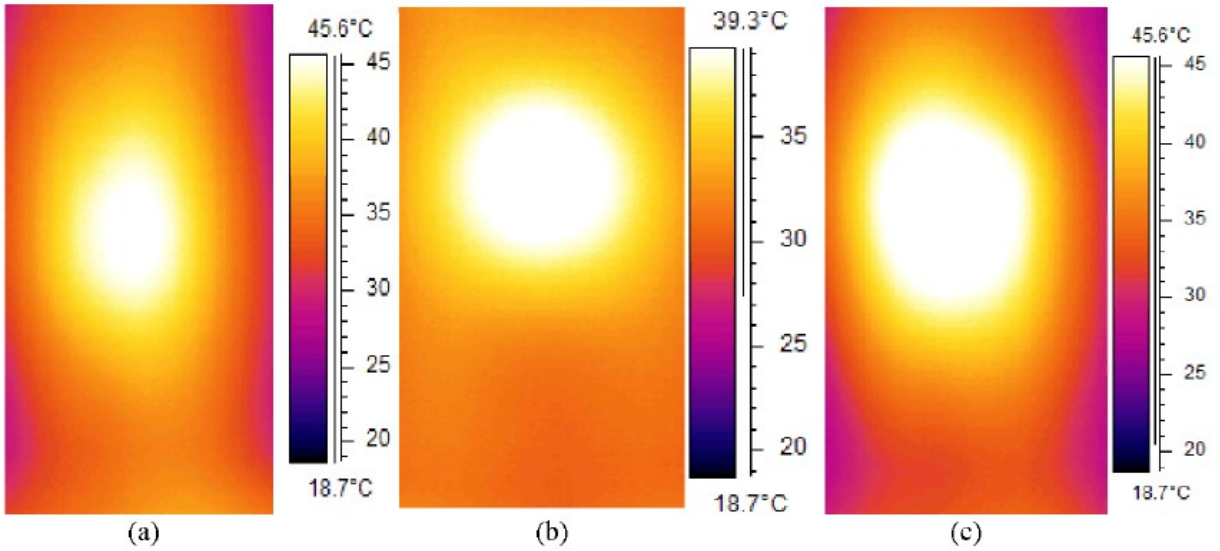

Figure 2.24: Air-filled debonds on CFRP wrapped cylinders (a) 1.4" x 1.4" specimen (b) 2" x 2" specimen (c) 3" x 3" specimen (Halabe et al. 2008).

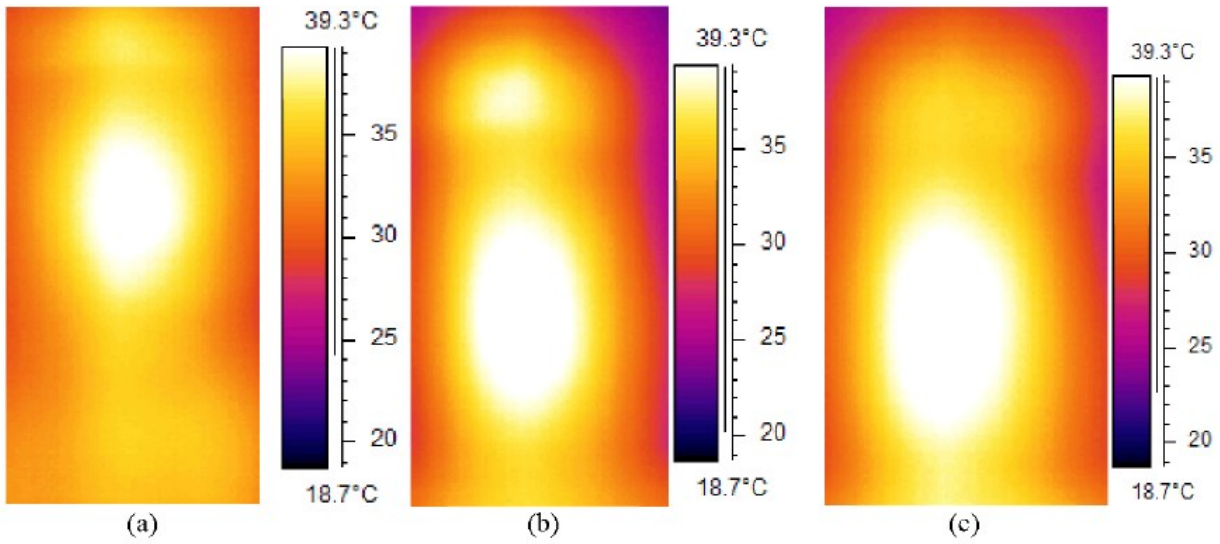

Figure 2.25: Water-filled debonds on CFRP wrapped cylinders (a) 1.4" x 1.4" specimen (b) 2" x 2" specimen (c) 3" x 3" specimen (Halabe et al. 2008).

Field Testing

Testing for the field side of this study was performed on a timber bridge in Moorefield, WV where the timber piles were wrapped with GFRP composite. Infrared thermography was employed to locate debonds and delaminations prior to the piles being wrapped with FRP. In order to obtain a temperature variance on the surface of the pile, researchers used a portable shop heater capable of producing 1500 W of energy to heat the surface. Due to site conditions, access to the piles was limited. Therefore, only two of the piles were evaluated using IRT. In the first pile a delamination within the pile was found. Evidence of this is shown in Figure 2.26 (a) that shows a visual image of the pile and Figure 2.26 (b) that displays a "hot-spot" or bright region in the infrared image. The temperature of the "hot-spot" was found to be 55.1 ^{0}C while the adjacent sound area was 44.5 ^{0}C. The presence of the delamination was confirmed by tap testing.

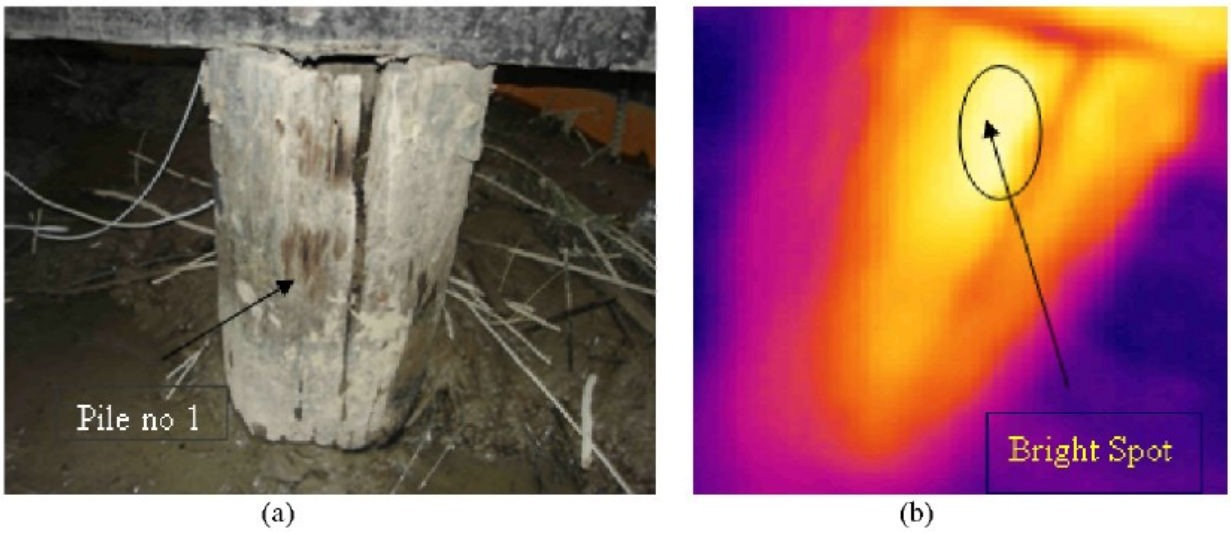

Figure 2.26: (a) Visual image of first timber pile (b) Infrared image prior to wrapping (Halabe et al. 2008).

A second and third pile were observed, however, site conditions limited infrared thermography to just pile two. The infrared image of the second pile indicates a debond is present due to the bright region within the image. Analysis of the image identifies the temperature of the "hot-spot" to be 59.1 ^{0}C with the sound region coming in around 40.9 ^{0}C. Again, tap testing supported this finding. The visual image and infrared can be seen in Figure 2.27 (a) and (b) respectively. Once the piles were wrapped with the GFRP composite, piles one and two were again

examined via IRT. As shown in Figure 2.28 (b), a bright region or "hot-spot" was found in the first pile with a temperature difference of 36.0 °C between the debond and defect-free region. However, this "hot-spot" was actually found to be a seam in the FRP. Tap testing conducted on the region confirmed that no debond or delamination was present. The same phenomenon occurred in pile number three in which a "hot-spot" on the infrared image was found to be a seam in the FRP. Figure 2.29 show the visual and infrared image of pile number three after the GFRP wrapped was installed.

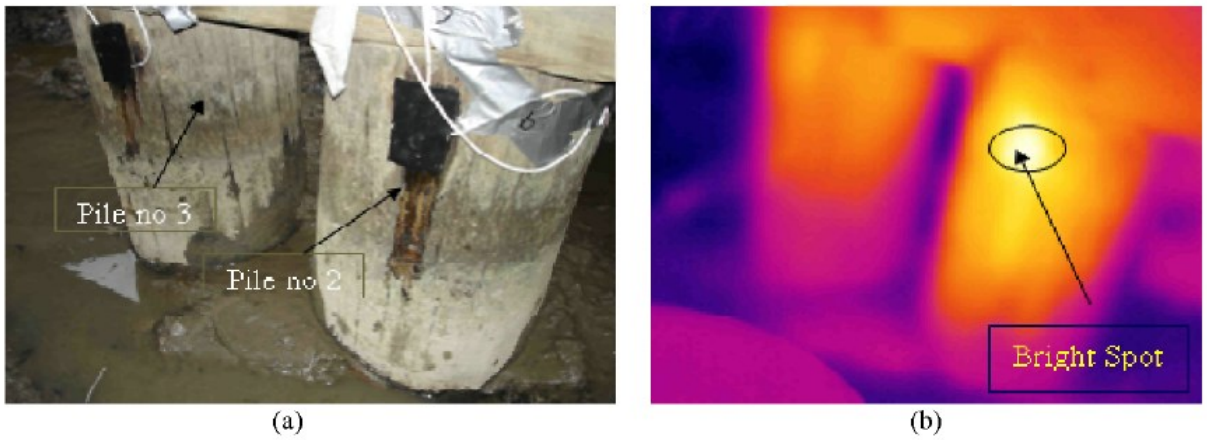

Figure 2.27: (a) Visual image of second & third timber piles (b) Infrared image of pile two prior to wrapping (Halabe et al. 2008).

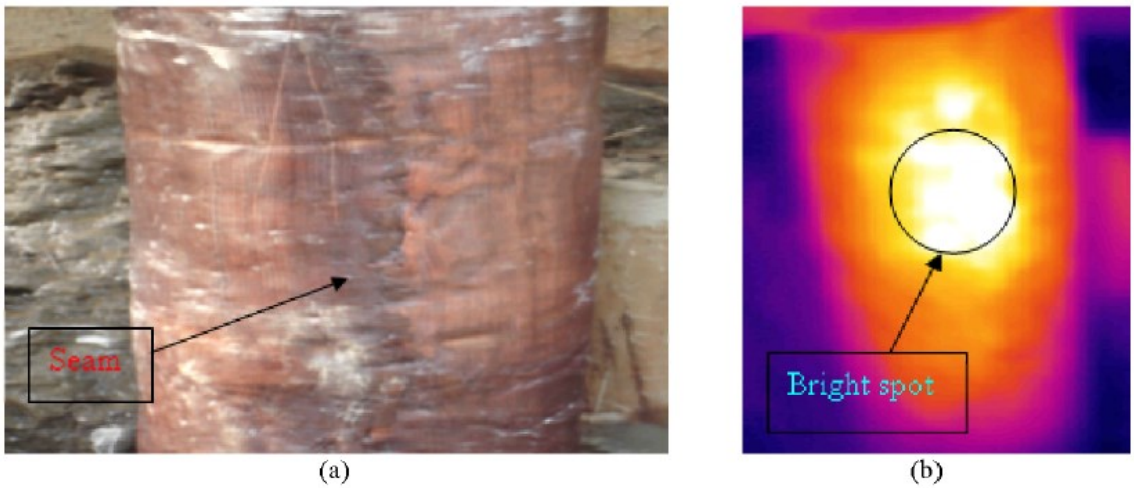

Figure 2.28: (a) Visual image of first timber pile with seam (b) Infrared image of first pile after wrapping (Halabe et al. 2008).

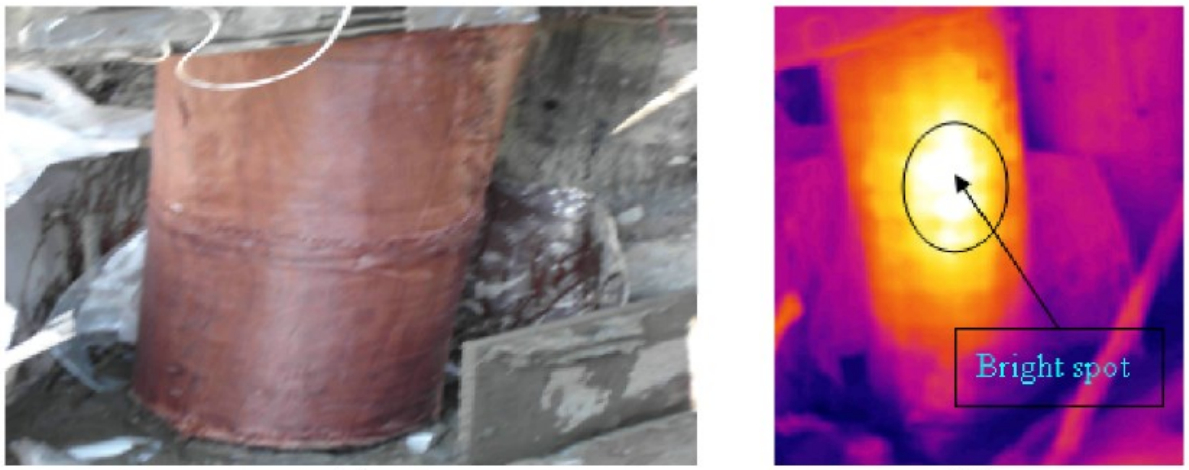

Figure 2.29: (a) Visual image of third timber pile with GFRP wrap (b) Infrared image of third pile after wrapping (Halabe et al. 2008).

Conclusions

This study was able to show that infrared thermography has the ability to successfully identify air-filled and water-filled debonds varying in size from 3" x 3", 2" x 2", and 1.4' x 1.4" in concrete column encased with either Carbon Fiber Reinforced Polymer (CFRP) composites wrap or Glass Fiber Reinforced Polymer (GFRP) composites. It was also revealed that the water-filled debonds appear as "hot-spots" if the wraps are thin enough. In addition to these findings, the field testing of the study was able to locate delaminations in timber pile prior to them being wrapped with GFRP with similar infrared thermography techniques as those used in the laboratory component. The data collected from the field also showed that the wrapping process was executed correctly since no subsurface debonds were identified. After examining these findings, it is apparent that IRT is an excellent quality control device both during the wrapping process and after for maintenance applications. IRT has the ability to identify potential debonds and delaminations while the components in question are in-service, and repairs such as resin injection can be performed to preserve the structural integrity of the structure.

2.3 FRP BRIDGE REHABILITATION

The following sections discuss how fiber reinforced polymers (FRP) have been implemented in the field of bridge rehabilitation, and how the application of FRP can be a cost effective solution to repairing dilapidated infrastructure.

2.3.1 FIELD PERFORMANCE OF FRP BRIDGE REPAIRS

(Stallings et al. 2000)

Introduction

During the period of when this paper was written over 50% of the bridges were constructed prior to 1940 and work conducted by Klaiber et al. (1987) estimated that 42% of those bridges were structurally deficient. With such a high volume of repairs needed, it is paramount to develop reliable and cost effective repair techniques. Previously, structures have been rehabilitated by adding beams to the structure or by mechanically fastening reinforcing plates. In many applications, steel is the material of choice for such reinforcement plates. Using steel has many disadvantages though, such as: corrosion of the steel, further deterioration of the bond at the steel-concrete interface, and the complexities involved with handling the material. In lieu of steel plates, externally bonded CFRP, GFRP, or aramid sheets have shown to be effective in strengthening bridges.

The intent of this research was to focus on the field application of FRP plates used to make repairs on an existing reinforced concrete bridge. Particular testing included quantitative measurements of vertical deflections, strains in primary flexural reinforcement, and strains on the surface of the FRP plates. Both static and dynamic testing was performed on the bridge before and after the FRP repairs were made. The bridge specimen belonged to the Alabama Department of Transportation (AL-DOT) and was constructed in 1952. Four reinforced concrete girders made up the superstructure. The bridge included seven simply supported spans with each span length equalling 10.36 m (33.98 ft). Visual inspection of the concrete girders revealed a developed system of flexural cracks with minor amounts of spalling along the surface of the girders. There was no

indication of corrosion in the reinforcement. Researchers intended to use FRP plates to mitigate the deterioration of the bridge from the widening of the flexural cracks over time.

Field Repairs

Experimental repairs were conducted on one span of the bridge. A combination of both CFRP and GFRP plates were used to make the repairs. Of the four girders, only three of them had FRP applied to them while the first girder served as a control. A CFRP plate was applied to the bottom of the girders while both sides had GFRP plates applied. The GFRP plates were added to reduce the bridge deflections and to resist opening of the flexural cracks by adding additional stiffness. Engineers sought a 20% increase in bending moment capacity with the addition of the CFRP. It is important to note that the FRP plates did not encase the entire girder. A cross-sectional view of the bridge with FRP placement is shown in Figure 2.30. The FRP plates were unidirectional with the fibers oriented parallel to the longitudinal axis of the plate. Both plate types consisted of six-ply uniaxial laminate, and the GFRP was a standard E-glass, while the CFRP was graphite/epoxy composite with a 60% fiber volume ratio. Based on prior experience, researchers elected to use Dexter-Hysol EA 9460 as the structural adhesive used to bond the FRP plates to the concrete surfaces.

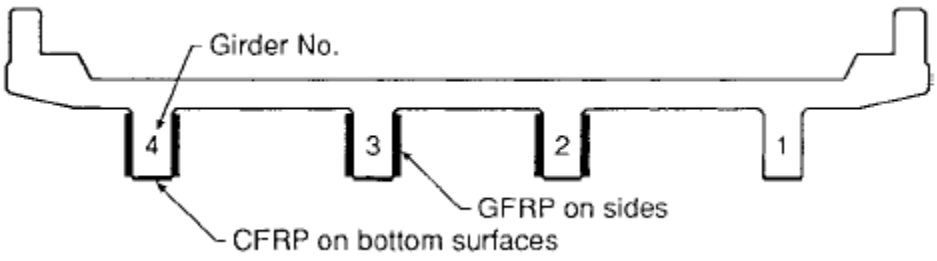

Figure 2.30: Cross-section of bridge with location of FRP plates (Stallings et al. 2000).

In order to achieve a strong bond between the concrete and FRP, the girders were prepped prior to the installation of the FRP plates. Surface preparation of the concrete girders involved taking a handheld grinder to remove “high spots” and to smooth out roughness created due to inconsistencies in the formwork. To expose the course aggregate, the girders were subjected to sandblasting. Finally, the girders were pressure washed with a solution of mild detergent and hot

water to remove any contaminates that may decrease the affinity of the structural adhesive. With respect to the FRP plates, they were prepared by using 100 grit sand paper on a handheld rotary disk sander to sand the contact surface of the plates. All surfaces in contact with the bonding epoxy were sanded and cleaned with methyl-ethyl-ketone.

Application of the plates to the girders was a multi-step process that first involved marking the location of the plates on the girders prior to attachment. Once the girders were laid out, the epoxy was mixed and applied to the plates. At this point in time, the plates were positioned on the girder and held in place while a vacuum bag was setup to apply pressure to the plates during the curing process of the epoxy. The plates were connected via butt joints with splice plates over lapping the butt joints. The plates were placed over one-third of the length of the girder. A vacuum pressure of 0.034 MPa was maintained over the entire surface of the FRP for at least six hours as required for the proper curing of the epoxy. For the period of one-week during the FRP application process, all bridge traffic ceased.

Conclusions

Static and Dynamic testing was performed on the bridge by a three axle truck provided by AL-DOT. Load tests were conducted before and after the application of the FRP plates. Testing showed that the use of FRP plates was successful in reducing stresses in the reinforcing bars anywhere from 4-12% during static loads tests, and 4-9% during dynamic loading. Deflections in the girders also saw a reduction. A reduction of 2-12% for static tests was observed while dynamic testing saw reductions ranging from 7-12%. Analysis of the cracked-section moment of inertia of the girder cross sections showed that application of the FRP plates increased the girder moment of inertia by roughly 5%. It is important to note that reductions in deflections and stresses in the rebar were greater in the three girders with GFRP plates applied than the one girder without the GFRP side plates. This phenomenon would imply that the use of GFRP plates are a cost effective rehabilitation solution to increase the stiffness of girders, while the CFRP plates can be reserved for the bottom of girders to enhance the load carrying capacity of the bridge.

2.3.2 APPLICATION OF FRP LAMINATES FOR STRENGTHENING OF A REINFROCED CONCRETE T-BEAM BRIDGE STRUCTURE

(Hag-Elsafi et al. 2001)

Introduction

This study showcases the collaboration between researchers and the New York State Department of Transportation (NYSDOT) on a demonstrative project involving the use of FRP components to repair concrete T-beam bridge girders. Transportation officials in New York were faced with similar problems that many of transportation officials are faced with: How do we repair bridges in a timely and cost effective manner? NYSDOT officials elected to participate in a demonstration project that involves increasing the flexural and shear capacities of the aforementioned concrete T-beams. Estimates had the replacement cost at approximately $1.2 million while costs associated with rehabilitation were estimated at $300,000, thus illustrating the cost-saving potential FRP rehabilitation has. Researchers wanted to measure how effective the FRP repairs would be in strengthening the reinforced concrete T-beams.

The project was centered on a bridge in the City of South Troy, Rensselaer County, New York. The simple span bridge spanned over Wynantskill Creek and was constructed in 1932. It is 12.19 m (40 ft) in length and is roughly 36.58 m (120 ft) wide. There are 26 reinforced concrete T-beams on 1.37 m (4.49 ft) centers. Figure 2.31 illustrates a transverse plan view of the bridge. Since opening, the bridge has been open without weight restrictions and sees an average daily-traffic volume of approximately 30,000 vehicles. The bridge has five traffic lanes, and is a crucial link between the City of South Troy and areas west of the Hudson River. In routine inspection, many of the T-beams in the bridge superstructure were observed to have freeze-thaw cracking and signs of concrete delamination. These results stemmed from excessive moisture and salt infiltration on the superstructure. The decision was made to rehabilitate the using FRP laminates since this methodology provided the least amount of traffic disruptions and was the most practical approach. Rehabilitation work involving scaffolding erection, surface preparation, and laminate installation was executed from August to November of 1999.

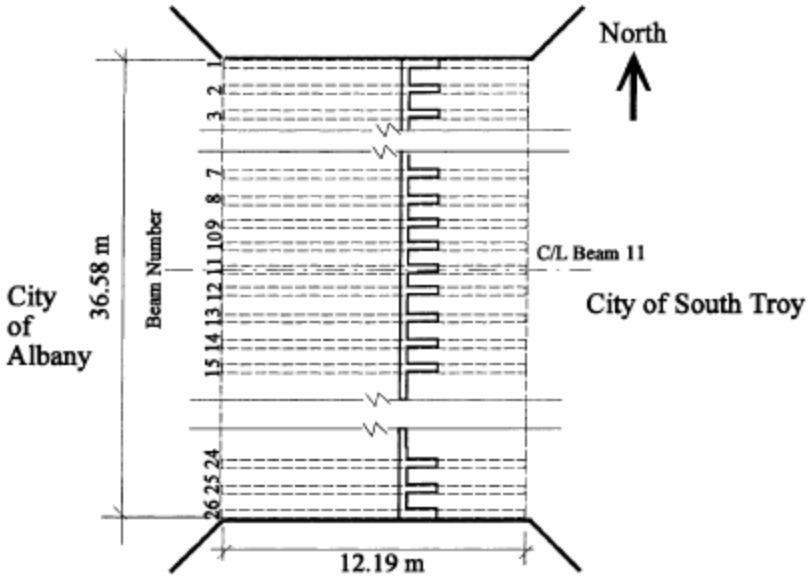

Figure 2.31: Transverse plan view of NYSDOT bridge (Hag-Elsafi et al. 2001).

FRP-laminate Design and Installation

Design of the FRP laminates was conducted by a third party in conjunction with the laminates' manufacturer. Flexural and shear capacities of the FRP system were developed based on the assumption that there was a 15% loss in the rebar area due to corrosion. Although this approach does not account for strain compatibility, the required area of laminate was calculated by the following equation: $A_1 = \frac{0.15(A_s F_y)}{F_1}$ where A_s and F_y are, respectively, the area and yield stress of reinforcing steel and F_1 is the design stress of the FRP laminate. The FRP laminates were a Replark System, and were comprised of Replark 30 unidirectional carbon fibers used in combination with a primer, putty and resin produced by the same manufacturer. In order to increase the shear strength of the webs, U-shaped CFRP strips known as U-jackets were installed to minimize the propagation of the freeze thaw cracking and contain further delaminations. These U-jackets were installed on the bottom and up the sides of the T-beams.

Installation of the FRP laminates first required that areas with delaminations and visible cracking to be repaired using a cementitious grout. Uneven surfaces were then ground smooth, and

the entire superstructure was then sandblasted and pressure washed with water to remove any loose surface materials. The locations of the laminates were then marked on the beams followed by the application of a primer and putty. The CFRP strips were 13" wide and were spaced 6" apart from one another. A total of two layers of FRP were installed on the beams. Figure 2.32 provides a visual representation of the proposed FRP system. Once the laminates were in place, an epoxy resin was applied to impregnate the laminate. In an effort to control curing temperatures, heaters were applied to the CFRP strips. After the laminates had cured, they were then painted with an ultraviolet resistive paint for protection. Figure 2.33 displays the FRP strips (a) before being painted and (b) after being painted.

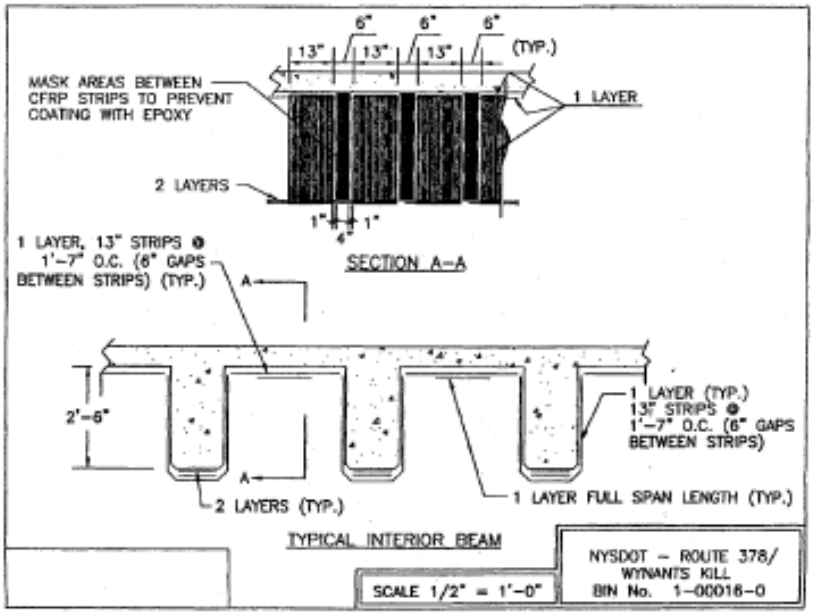

Figure 2.32: Proposed plan for FRP laminate installation (Hag-Elsafi et al. 2001).

(a) (b)

Figure 2.33: (a) Installed CFRP strips (b) Painted CFRP strips (Hag-Elsafi et al. 2001).

Conclusions

Load testing of the bridge consisted of tests before and after the installation of FRP laminates. Load tests were conducted by using four different load trucks with an average weight of 196 kN (approximately 44,000 lbs). Both before and after testing involved subjecting the bridge to seven different load cases or sequences. In addition to the seven load cases, after the FRP was applied, an eighth test was performed. This test had all four trucks parked back-to-back to maximize the load effects on the bridge. The total induced moment on the bridge due to this test was 2.75 times the moment created by the MS18 loading. All in all these tests discovered that after the CFRP stripes were installed stresses in the main reinforcement were moderately reduced while the concrete stresses saw a moderate increase. Loading of the bridge after rehabilitation also revealed that transverse live-load distribution amongst the beams improved slightly. Researchers also observed a downward movement of the neutral axis after the FRP laminates were installed when compared to the location of the neutral axis prior to repairs being made. The overall achievement of the FRP laminates in strengthening this bridge along with minimal disruptions in traffic flow meant that the NYSDOT was successful in demonstrating that FRP rehabilitation techniques can indeed be a cost efficient alternative to many infrastructure related problems.

2.3.3 USE OF EXTERNALLY BONDED FRP SYSTEMS FOR REHABILITATION OF BRIDGES IN WESTERN CANADA

(Hutchinson et al. 2003)

Introduction

Through numerous field application project across Canada the Intelligent Sensing for Innovative Structures (ISIS) Canada research network was involved in nondestructive testing and structural health monitoring, and they have established design procedures and standards for the rehabilitation of concrete structures using fiber reinforced polymer materials (FRP). This paper functioned as a review of four recent rehabilitation projects employing externally bonded FRP to bridge structures. The four projects each involved different strengthening requirements. The Country Hills Boulevard Bridge in Calgary utilized CFRP laminates to increase the flexural strength. Two other bridges including the Maryland Bridge in Winnipeg, Manitoba and the John Hart Bridge in Prince George, British Columbia made use of CFRP sheets to enhance the shear strength of I-shaped AASHTO girders. CFRP sheets were again used to strengthen concrete bridge corbel supports on the Jaques Lodge Pedestrian Bridge in Calgary, Alberta. Visual inspections of the bridges have been conducted on a regular basis, and many of the findings are discussed and listed by the researchers.

Field Observations

Country Hills Boulevard Bridge

The City of Calgary sought to strengthen the bridge to support current design live loading with the stipulation of maintaining at least one-lane of traffic on the bridge during all phases of construction. This particular bridge is a two-span composite steel box-girder superstructure with a 44^0 skew, and was also designed for the AASHTO HS20-44 loading. Each of the three box-girders are 1.575 m (5.16 ft) wide, 1.67 m (5.47 ft) deep, and support a 140 mm (5.5 in.) thick deck with a 50 mm (1.96 in.) asphalt wearing surface. Both spans are 57.9 m (189.96 ft) long with an overall width of 10.06 m (33 ft). The deck spanned 1.575 m (5.16 ft) between the box-girders and proved to be problematic, thus creating a need for rehabilitation. A finite element grid analysis program

was used to model the bridge performance under a moving CS-750 live load. Analysis showed that the strength of the slab was not the problem, but rather an increase in the negative bending moment reinforcement was required. In two different locations in each span the factored negative bending moment exceeded the moment carrying capacity of the existing reinforced slab. Engineers and researchers proposed two different solutions to the problem. One proposed method included placing slotted strips in the deck and strengthening these slots with additional reinforcement. The second solution involved adding epoxy bonded carbon fiber strips to the top of the deck slab. Such CFRP strips would be applied in the tension deficient zone and anchored to the nearest compression zone.

Strengthening of the concrete deck involved the installation of Sika Dur CFRP strips that were 100 mm (3.93 in.) in width and were 1.2 mm (0.047 in.) thick. The strips were placed on 500 mm (19.685 in.) centers in areas requiring additional strength. Design of the rehab limited the strips to less than 25% of their ultimate capacity. The exact number of strips that were used was not mentioned in the published paper, however, enough strips were used to limit the capacity of the strips to 25% during ultimate loading conditions. The strips were extended beyond the tension zone and terminated in compression zones of the slab on either side of the tension zone. Figure 2.34 shows the CFRP strips on the existing deck slab as the new deck is being poured on top of the strips.

Figure 2.34: CFRP strips applied to existing deck (Hutchinson et al. 2003).

John Hart and Maryland Bridges

Together, the John Hart Bridge in Prince George, British Columbia and the Maryland Bridge in Winnipeg, Manitoba were comprised of I-shaped prestressed concrete AASHTO girders which did not meet the modern shear strength capacity due to both bridges experiencing heavier truck loads. Since the bridges were constructed in the early 1960's, the Gross Vehicle Weight (GVW) of trucks using the bridges has increased by a factor of three. Both bridges serve on arterial roadways, and must remain open during repairs.

The John Hart Bridge contained seven simply supported spans each with a length of 33 m (108.268 ft). There were six 1500 mm (59 in.) deep prestressed girders in each span. Each end of the 42 girders was reinforced with a single layer of diagonal Replark CFRP sheets placed over 4 m (13.12 ft) distance from the end supports. By incorporating the CFRP sheets the shear capacity of the girders was increased by approximately 15-20%. After installation, all of the sheets were covered with a 2-4 mm (0.078-0.157 in) protective coating. In total there were 84 areas that the CFRP sheets were applied, and the entire rehabilitation was completed in a six-week time frame

through September and October of 1999. Figure 2.35 shows the John Hart Bridge and Figure 2.36 displays the CFRP sheets being applied.

Figure 2.35: John Hart Bridge, Prince George BC (Hutchinson et al. 2003).

Figure 2.36: Application of the CFRP sheets (Hutchinson et al. 2003).

In an effort to strengthen the shear capacity of the Maryland Bridge, the City of Winnipeg, Manitoba, Canada completed a trail run using CFRP sheets. As with the John Hart Bridge, the Maryland Bridge consisted of two prestressed concrete girders that were continuous across five spans. Rehabilitation involved two separate companies working on either end of the bridge and using two different materials. One side of the two girders were strengthened by the Replark system while the other ends were repaired using the Mbrace system. The recommended design called for the CFRP sheets to be installed vertically with a horizontal layer at the top and bottom of the web. This ultimately led to an increase of 20-25% in the girders' shear capacity. The horizontal stripes helped to resist the outward peeling force of the CFRP created by the shape of the girder. This force was also accounted for in the overall design. Experimental tests showed that the CFRP shear contribution can simply be added to that of the concrete and the stirrups to arrive at the overall shear capacity of the girder (Hutchinson et al. 1999). Figure 2.37 represents the vertical and horizontal CFRP strips after they were installed.

Figure 2.37: CFRP strips installed on the Maryland Bridge (Hutchinson et al. 2003).

Jaques Lodge Bridge

The Jaques Lodge Bridge is a pedestrian bridge located in Calgary, Alberta. This particular bridge is constructed of a precast concrete girder that is "dropped in" and supported on both ends by a cantilevered girder. The concrete corbels that supported the main girder showed cracking that originated from unexpected frictional forces and a lack of internal diagonal reinforcement. Figure 2.38 represents a close-up of one of the corbels in reference to the global location on the bridge.

Figure 2.38: Cracking of a corbel on the Jaques Lodge Bridge (Hutchinson et al. 2003).

Engineers chose to use a strut and tie model for the basis of design of the CFRP rehab, and the strains in the CFRP sheets were held to a maximum of 4 millistrains. To achieve a thorough repair, the entire main span girder was lifted up off of the corbels. This allowed applicators to clean and prep the surface of the concrete. Once the surface preparation was completed, Replark CFRP sheets were again used to make the repairs. A combination of one horizontal layer and one diagonal layer was applied to both sides of the corbel as shown in Figure 2.39. Once the epoxy used to impregnate the FRP was cured, a protective coating was applied and the man span girder was lowered back down. Figure 2.40 shows the bridge after repairs were made. Repairs to the bridge lasted for six weeks.

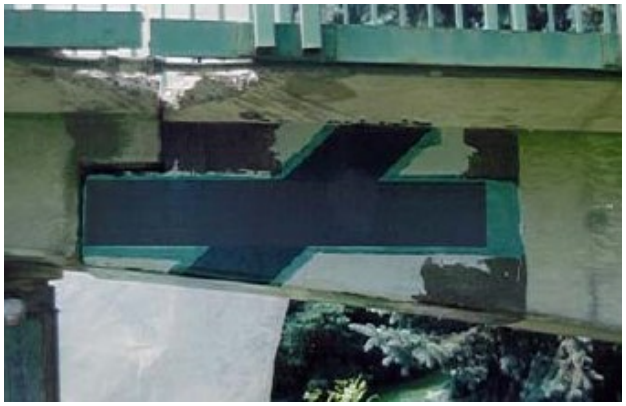

Figure 2.39: CFRP sheets applied in the horizontal and diagonal direction (Hutchinson et al. 2003).

Figure 2.40: Jaques Lodge Bridge after corbel repairs (Hutchinson et al. 2003).

Conclusions

In four separate cases, carbon fiber reinforced polymer (CFRP) sheets have been externally bonded to various bridge components ranging from the superstructure to the bridge deck. The ease at which the CFRP materials could be applied meant that all four projects saw a reduced construction/repair time when compared to conventional techniques. Three of the four projects discussed here involved heavily traveled highway bridges where at least one lane of traffic was open at all times during rehabilitation. In most of the cases discussed, the application of the FRP products increased either the shear or bending strength by a considerable amount. When combining the success of the strengthening abilities with the ease of installation, ISIS Canada research network has demonstrated how successful FRP can be in practical applications.

3. TURNPIKE BRIDGE FIELD REHABILITATION

3.1 BACKGROUND

The field study on the application of FRP wraps and the nondestructive testing evaluations of the wraps was conducted on WVDOH project number S310-15-10.14 00, also known as the "Turnpike Bridge." The project entailed a joint operation between WVDOH and WVU-CFC, where WVU-CFC would handle the design and quality assurance aspects of the project, while WVDOH would oversee the actual repairs and wrap installation done by an outside contractor. The involvement of WVU was crucial to the overall success of the project because this project marked the first time that WVDOH would let the field work to a general contractor. In previous FRP wrapping work conducted by WVDOH and WVU-CFC, graduate students with CFC would execute the field work alongside members of WVDOH. Projects such as the Madison Avenue Bridge in Huntington, WV (GangaRao et al. 2015, Halabe et al. 2014) were used as research style projects to further illustrate the usefulness and effectiveness of FRP rehabilitation to WVDOH. This chapter of the report provides an in-depth analysis and description of the repairs made to the bridge substructure by a WVDOH Contractor under the design supervision of Dr. Hota GangaRao, WVU-CFC. Understanding of this repair process is crucial to appreciate the use of field nondestructive testing described in Chapter 4.

The Turnpike Bridge was located along Interstate 77 (WV Turnpike) between Charleston and Beckley, West Virginia. The highway serves as the main corridor from West Virginia to Virginia. The bridge spans both north and southbound lanes of Interstate 77 and is a component of Milburn Road linking East Kingston to Kingston, WV. The bridge is comprised of three sets of piers with each pier containing three columns for a total of nine columns. A plan sheet illustrating the layout of the piers and columns with respect to the interstate can be seen in Figure 3.1. Due to the placement of the piers 1 and 3 being in the ditch line adjacent to the interstate, the columns were in close proximity to the shoulders of the roadway. This meant that during periods of snowfall throughout the winter months, columns in piers 1 and 3 were exposed to high volumes of road salt and water thru splashing.

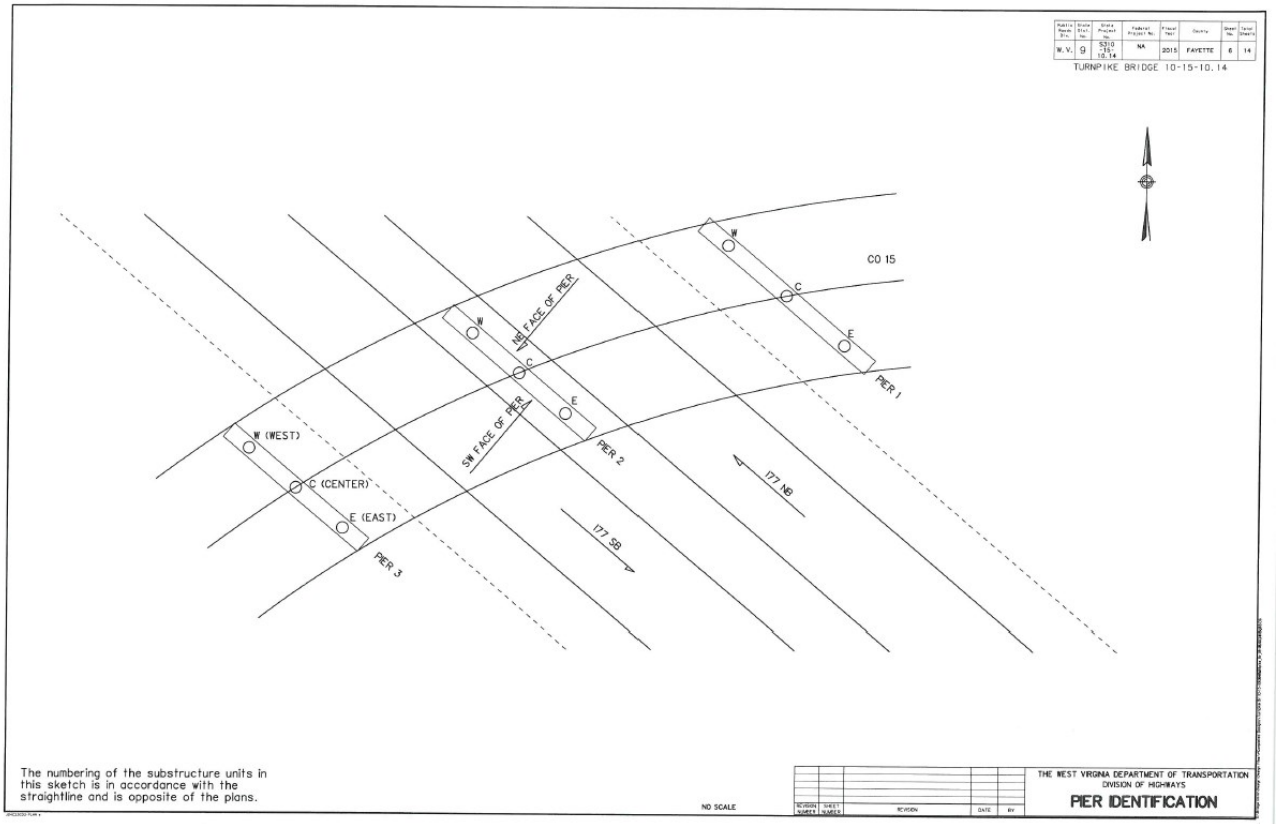

Figure 3.1: Plan sheets depicting the layout of the Turnpike Bridge.

As a result of exposure to increased amounts of deicing chemicals, the concrete elements of the columns began to spall. Throughout the course of time the water and salt reached a depth into the column equivalent to the depth of the rebar stirrups. Eventually, the stirrups began to corrode, thus, accelerating the spalling process through the expansive properties of the iron oxides (Choi et al. 2014). Spalling of the concrete ultimately reached a point where WVDOH had to initiate repair and preventative maintenance measures. Evidence of the severity and extensiveness of spalling prior to the contractor removing additional unsatisfactory concrete is shown in Figures 3.2 and 3.3, and is denoted by the red rectangle in Figure 3.2. Stirrups exposed to various environmental conditions are observed to be darker in color due to prolonged corrosion and exposure.

Figure 3.2: Extent of original concrete spalling.

Figure 3.3: Concrete spalling on pier 3.

Columns within pier 2 were shorter than columns in piers 1 and 3 due to the fact that the columns in pier 2 sit on top of the parapet wall dividing the north and southbound lanes. Although columns within pier 2 were not exposed to the high volumes of splashing that piers 1 and 3 experienced, the columns still exhibited spalling due to the sustained exposure to numerous environmental conditions. However, the spalling for these columns was concentrated near the bottom third of the columns directly adjacent to the parapet wall.

Due to restrictions imposed by the West Virginia Turnpike Authority, anytime work was conducted on Pier 2, both the northbound and southbound fast lanes had to be shut down for traffic.

For this reason, concrete repairs were made to piers 1 and 3 during the daytime, and repairs were made to pier 2 during night time operations.

3.2 Concrete Repairs

Crews with Titan Industrial Services, the general contractor awarded to conduct the work, began the repairs by first establishing with WVDOH the areas of concrete that needed to be removed and replaced. Original quantities provided at the time of bid called for 346 square feet of concrete patching to be completed prior to FRP wraps being applied. Once the contractor arrived on-site and began to remove the deteriorated concrete, it was found that more of the column had experienced spalling, and the justification was made between the contractor and the WVDOH to remove the additional concrete via a written change order. Reports from the WVDOH indicated that the final square footage of concrete patch work was nearly double the initial amount. Figure 3.4 illustrates the extent of the patching to be completed on pier 3, and Figure 3.5 displays the areas to be patched on pier 1. A large portion of the additional concrete patching stemmed from the quantities of "unsatisfactory" concrete on the interior side of the rebar stirrups. The extent of the patchwork also included patching elements approximately two feet below grade on piers 1 and 3 as depicted in Figure 3.6.

Figure 3.4: Pier 3 prior to patchwork.

Figure 3.5: Pier 1 prior to patchwork.

Figure 3.6: Excavation for patchwork.

Upon the completion of removing all of the deteriorated concrete, the reinforcing steel had to be cleaned and coated with a corrosion inhibitor to prevent further corrosion. The process of coating the steel is time consuming because the inhibitor has to be brushed on to ensure that all of the rebar is covered. Figure 3.7 is an image of the reinforcing steel after the corrosion inhibitor is applied at which point the rebar is light grey in color. Once the rebar was sufficiently covered, the process of patching the concrete could commence. The irregular shapes of the areas to be patched in addition to the columns being round made forming patches in preparation for pouring of the concrete cumbersome. Thus, the contractor had to develop unique forming methods that involved strapping half of a three foot diameter sonotube to the column to act as a form for the concrete. The formwork would have a notch in the top where concrete could be poured into the form. The contractor chose to use a high strength MasterEmaco repair mortar in place of the deteriorated concrete. Images of the formwork and patches after the columns were repaired can be seen in Figures 3.8 and 3.9 respectively.

Figure 3.7: Rebar with corrosion inhibitor.

Figure 3.8: Concrete formwork

Figure 3.9: Concrete patchwork.

3.3 Application of FRP

Initial FRP design for this bridge was conducted a few years prior to the release and execution of the actual work. Because of this, by the time the work was scheduled to start, the columns had deteriorated to the point that an additional two layers of FRP were added. The project specification sheet now called for a total of four layers of GFRP. The purpose of the FRP was to essentially provide a non-structural protective membrane around the columns while simultaneously enhancing the load carrying capacity of the bridge through increased confinement. FRP specifications called for a bi-directional, equal weight, 0°/90° fabric with a minimum tensile strength of 30 ksi and a Modulus of Elasticity of 2,200 ksi (ASTM D3039). The minimum

thickness required of the laminate was 0.04 inches/ply with the glass fabric yielding a weight of at least 26 oz. per square yard.

The FRP applicator/contractor, Titan Industrial Services, utilized a wet-lay-up methodology to install the glass fiber reinforced polymer (GFRP) wrap that ultimately provided increased flexibility in the wraps. Pre-impregnating the fabric with an epoxy or resin allows the fabric to closely follow the geometric shape of the structure being rehabilitated. For this project, the concrete substrate, and subsequent wraps, were treated with a primer specified by the FRP manufacturer prior to the installation of the original layer and top three layers. The primer is crucial to the success of the rehabilitation because the primer enhances the bond between the concrete and the FRP. The primer creates an adhesive layer that is similar to the matrix of the composite, and essentially forms a primer/resin continuum between the composite and concrete or masonry substrate. Thus, the curing of the primer and FRP is critical to the overall performance of the rehabilitation process.

Members of Titan's team experienced difficulty with the primer composite matrix on pier 2 when they experienced low temperatures during night time operations. Chapter 4 of this report includes more detail as to the impact the temperatures had on the performance of the wraps. Ambient temperatures above or below a specified range can affect the primers and resins by accelerating or reducing the time needed for the primers/resins to cure. While different manufacturers' may vary in their range of temperatures, the overall consensus is that the ambient temperature shall be between 55°F and 95°F for the application of resins, primers, and composites. The relative humidity should also be less than 85%. At too high of temperatures, and the primers and resins cure rapidly, thus decreasing the workability time. If temperatures are too low, then the inverse occurs and the products take longer to cure. Since environmental conditions such as temperature impacts the overall success, it is easy to see how minute changes in the in situ application can have a large effect on the composites.

State imposed installation procedures for this bridge called for a minimum of 4 layers of FRP with bi-directional (0°/90°) fiber configuration. The contractor elected to wrap the columns circumferentially and maintained a minimum of two inches overlap between adjoining wraps in

the vertical direction. Also, each end of a new wrap would overlay the point of origin by at least six inches in the horizontal wrapping direction. The wrapping process would continue up the column from the bottom to the top until the entire column had one layer of FRP. This operational system was repeated until each column was encased in four layers of FRP. It is important to note that the wraps were installed from the bottom of the column (a distance two feet below grade) to the top of the column. This method of application will aid in the prevention of water intrusion between the FRP wraps. Once a column was considered complete with respect to applying the FRP, members of WVU-CFC research team would conduct nondestructive tests on the composites to evaluate the adhesion or bonding of the wraps to each other and the concrete substrates. Results of the tests are discussed in later chapters of this report. Members of our team had only a narrow window of time (typically 2~3 days) to conduct the tests because the columns were only allowed to be exposed for seven days. Glass fabric composites such these wraps are subject to degradation via UV rays from sunlight (Cromwell et al. 2010). After the wraps on a column were completed, they had to be painted with a UV resistive paint that typically was an acrylic base or equivalent. An example of a completed column and pier set is shown in Figure 3.10 which represents a completed pier 3.

Figure 3.10: Completed Pier Set.

4. NONDESTRUCTIVE EVALUATION OF THE WVDOH TURNPIKE BRIDGE

The intent of this chapter is to describe the nondestructive testing conducted on the West Virginia Department of Highways (WVDOH) owned Turnpike Bridge Substructure Restoration project located in Fayette County, West Virginia. The reinforced concrete (RC) columns were an excellent candidate for rehabilitation with glass-fiber reinforced polymers (GFRP) fabrics due to the vast amount of concrete spalling. The details of the bridge and results of the nondestructive field evaluation are presented in this chapter. Several nondestructive testing techniques including the use of a digital tap hammer and infrared thermography were utilized for the evaluation of the GFRP wraps after installation. Evaluation included the detection of underlying debonds in the wrapped members. Furthermore, because the GFRP wraps were non-structural, the observed defects were identified and filled with resin by the WVDOH contractor. This chapter presents detailed findings showing the digital tap hammer and infrared results based on field measurements.

4.1 DESCRIPTION OF THE BRIDGE

The Turnpike Bridge in West Virginia is a two-lane bridge that is part of County Route No. 15 in Fayette County between Charleston and Beckley. The bridge crosses Interstate 77 which is a four-lane interstate that serves as the main thoroughfare between Charleston and Beckley Figure 4.1 (b) shows the location of the project with respect to Fayette County and Interstate 77. The bridge is supported at each end by concrete abutments and intermediately by three sets of piers (Piers 1, 2, and 3). Within each pier set, there are three columns (East, Center, and West) with pier caps to tie the three columns together. Figure 4.2 shows a picture of the bridge indicating the three pier sets and the three columns in each set. Columns in piers 1 and 3 were approximately 20 feet in height and were located in the ditch line on both sides of Interstate 77. Pier 2 columns sat in the middle of the north and southbound lanes on top of the parapet wall and were roughly 11 feet tall. The location of the columns in piers 1 and 3 put them in close proximity to the shoulder of interstate. This meant that during periods of snow removal the columns were exposed to high volumes of moisture and salt. Snow plows and traffic would splash salt and snow onto the columns

as they passed beneath the bridge. Through time the excessive splashing produced cracking that eventually yielded spalling of the concrete and corrosion of the rebar stirrups. Images of the damage prior to repairs can be seen in Figures 4.3 and 4.4. Damage to the piers was so severe that the rebar stirrups were extensively corroded and were clearly visible due to the spalling of loose concrete. Once the concrete was repaired, the contractor wrapped the columns with four layers of GFRP to create a protective cover over the columns.

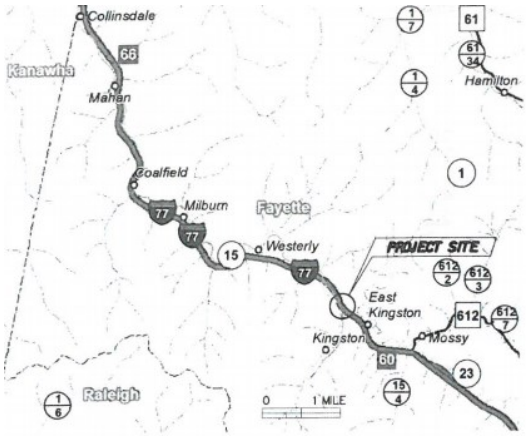

Figure 4.1: (a) Location of the project site provided by WVDOH

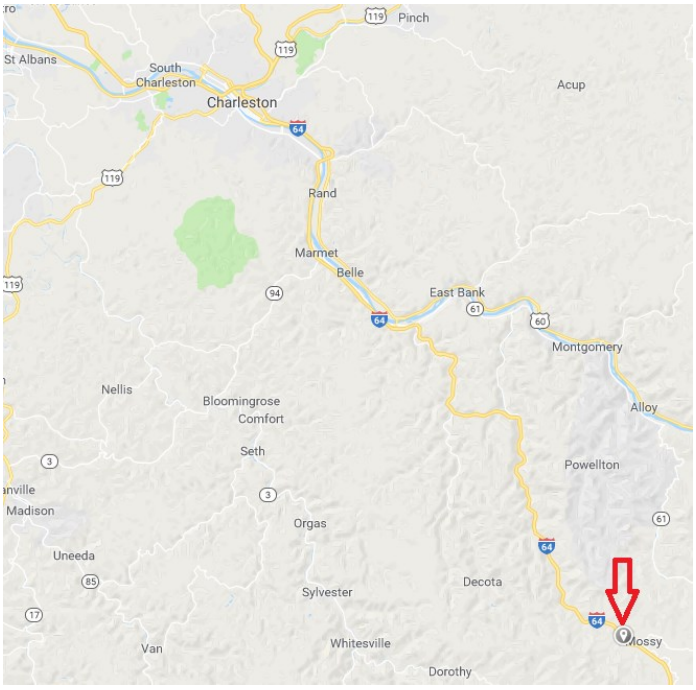

Figure 4.1: (b) Represents the location of the project with respect to Charleston, WV as indicated by the red arrow.

Figure 4.2: Pier identification.

Figure 4.3: Concrete spalling prior to rehabilitation.

Figure 4.4: Corrosion of the stirrups on one of the columns.

4.2 TESTING EQUIPMENT

Two types of equipment were used by Constructed Facilities Center (CFC) to analyze the integrity of the GFRP wraps. Those two types included a digital tap hammer as shown in Figure 4.5 and an infrared camera. Figure 4.6 (a) shows the portable infrared camera which was used for the field testing in conjunction with a shop heater Figure 4.6 (b). The heater was a 1500W quartz heater consisting of two heating rods. The heater could provide high intensity heat with uniform heating by moving it back and forth over the surface in question. The surface of the columns were heated approximately 45-50 seconds before they were examined using the infrared camera.

The tap hammer was manufactured by WichiTech Industries, Inc. It is a Rapid Damage Detection Device (RD^3) digital (electronic) tap hammer. The accelerometer in the hammer

translates the force-time pulse at the hammer head after each tap into a voltage pulse. The hammer receives the signal, and measures the pulse amplitude and pulse width at half-amplitude. The width of the force-time pulse correlates to the mechanical impedance of the structure being examined. A delamination in the GFRP, or a debond between the GFRP and the concrete, will reduce the local stiffness, and produce a wider force-time pulse. Therefore, deviation from nominal width indicates a debond is present (Georgeson et al. 1996). It is important to remember that the digital tap hammer measures only local defects and not global defects.

For the purpose of this research "good regions" were denoted as regions having tap hammer readings of 1100-1150μs. This range was established for FRP wraps on a concrete substrate via previous laboratory and field work conducted by fellow researchers at WVU. Other materials such as steel and timber could produce different readings indicative of a "good region". The tap hammer used during field testing produced approximately a 3% normal distribution amongst readings taken at the same location. This means that if multiple readings were to be taken from the same location, one would notice roughly a 3% difference in each of the readings. Readings that are above this normal variation, typically at least 10% higher, can be considered as indicative of subsurface defects. While the digital tap hammer has many advantages including easy to use, handheld, cost effective, etc., the device does have some drawbacks. For example, accessibility to the specimens being examined is crucial. Although the RD^3 is small and handheld, a user must have good access to evaluate the composite structure. In addition, the tap hammer is only used to identify defects or delaminations near the surface of composites. Previous research found that the tap hammer was only able to detect debonds to a depth of 6 mm (Georgeson et al. 1996). Thus, another nondestructive testing method such as infrared thermography needs to be employed to thoroughly analyze composite structures.

The camera used here is an InfraCAM SD™ infrared camera manufactured by FLIR Systems. The camera measures the infrared radiation emitted from an object and converts it to an equivalent temperature value in accordance with the Stefan-Boltzmann law. The thermal images that the camera produces are directly saved on a SD memory card which stores images in standard radiometric JPEG format. The InfraCAM SD™ infrared camera is capable of detecting infrared radiation in the spectral range of 7.5 to 13 microns. The camera is capable of making temperature

measurements in the range of -10°C to +350°C (+14°F to +662°F). The thermal images of InfraCAM SD™ are clearly displayed on the large 3.5" color LCD screen. The minimum focus distance of the infrared camera is 0.3m. Thermal sensitivity of this infrared camera is 0.1°C. The images that the camera produces can be analyzed either in the field by using the real-time spot temperature measurement marker built into the camera software, or in a computer using FLIR Systems QuickReport software. The spot temperature measurement option of the software enables temperatures to be measured at any point in the field or in the laboratory. The area feature provides average temperature over a small area and has the advantage of minimizing the random noise associated with the various pixels.

It is important to note that this field application has focused on the use of low cost nondestructive testing equipment. The RD^3 digital tap hammer costs about $1500 and the InfraCAM SD™ is a low-cost infrared camera with a price tag of less than $4000. The shop heater costs about $60. While the total nondestructive equipment cost is under $6000 (as opposed to $60,000 for high end infrared systems), the subsequent field testing results will demonstrate that this set of nondestructive equipment is very effective for evaluating the condition of the FRP wraps and taking immediate remedial action when subsurface debonds between the wraps and underlying concrete are detected.

Figure 4.5: Digital Tap Hammer

(a) InfraCAM SD™ infrared camera

(b) Shop heater

Figure 4.6: Infrared testing equipment

4.3 PIER 3 FIELD TESTING (JULY 18, 2017)

The objective of the nondestructive testing was to detect any debonds or underlying defects in the repaired concrete columns. Due to schedules set by the contractor, only pier 3 was tested on July 18, 2017. The average temperature that day during testing hours of 11:00 A.M. and 4:00 P.M. was 25°C (77°C) and it was a clear sunny day. Upon arrival at the pier each column was first visually inspected for any noticeable debonds. Next, each column was tested using the digital tap hammer beginning at the bottom of the column and working towards the top of the column in a spiral fashion. As defects were found, they were marked using chalk and measured for size. Per project specifications, the contractor was allowed debonds up to 2 in^2. An example of marked debonds can be seen in Figure 4.7. Note the hole drilled into the debonded region is to allow injection of resin into the debond. Regions of GFRP with tap hammer readings outside the good range that was established at the beginning of testing for each column were noted and documented. Detailed results of the tap hammer readings are presented in Appendix A of this report. It is important to note that there were several regions on all three columns of pier 3 that were injected with resin immediately prior to testing. The resin was still wet at the time of testing, thus these

areas were marked and the contractor was advised to monitor those areas to ensure they were completely filled.

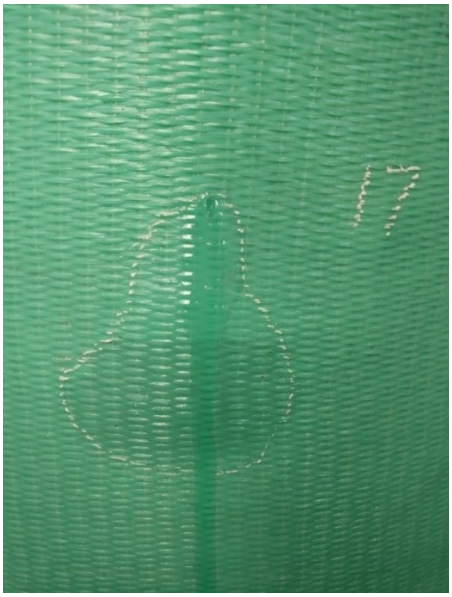

Figure 4.7: Example of a debond found using digital tap hammer techniques.

Once the debonds were outlined by means of digital tap hammer testing, infrared thermography was used to further inspect the areas of concern. For detecting the subsurface defects, it was necessary to heat the columns using the shop heater prior to acquiring the infrared images. The heater was moved back and forth from a distance of approximately 1 ft over the surface of the debond in order to ensure uniform heating. The heating time for each location was about 5 minutes as the test areas had been exposed to the sun most of the afternoon. After the heat source was removed and the infrared image was acquired, the areas with debonds showed up as hot spots (areas with higher temperatures) compared to the surrounding areas that are defect-free. Debonds were classified as regions where temperatures were at least two degrees Celsius higher. This is because the regions with debonds do not conduct heat as quickly as compared to those regions which are defect-free. Thus, the surface temperature above the debonds is higher. Infrared testing was limited to the bottom third of the columns because the only access to the upper portion of the columns was by ladder. The process of heating the surface would be too cumbersome to safely complete off of the ladder. So these upper areas of the columns were tested only using the digital tap hammer.

Examples of regions with elevated digital tap hammer readings for the east column in pier three are shown in Figure 4.8. These points were denoted as points 17 and 33 representing the point in time at which they were found. When nondestructive testing was initiated on a column, debonds were identified in sequential order (i.e., the first debond was labeled as point 1 and so on). Members of the team would begin at the bottom of the column and work their way around the column until they reached the origination point. This process would continue towards the top of the column as each circumferential pass was completed. The numbering scheme continued in a chronological fashion for each pass. After the completion of the first circumferential pass, the numbering would not reset, it would simply start where the previous pass finished. Figure 4.9 depicts the infrared images associated with points 17 and 33 shown in Figure 4.8. As shown, the difference in temperature is greater than two degrees C, thus, indicating a debond is indeed present. An even larger debond is shown in Figure 4.10 where the infrared image is shown for the seventeenth point of concern on the center column of pier 3. This is also the same point isolated in Figure 4.7. The results clearly confirm that a debond is present due to the high difference in temperature.

Area 13 on the center column of pier 3 is displayed in Figure 4.11. The area in question is along a joint in the outer layers of GFRP. An Illustration of area 13 shown in Figure 4.11 and the debond that is present can be seen in Figure 4.12. A Representation of tap hammer areas of concern and infrared readings for the west columns are exemplified in Figures 4.13 and Figure 4.14 respectively. With more than 2 degrees of separation, a debond is clearly evident. Additional tap hammer results for pier 3 are represented in Figure 4.15 with the infrared results shown immediately afterwards in Figures 4.16 and 4.17.

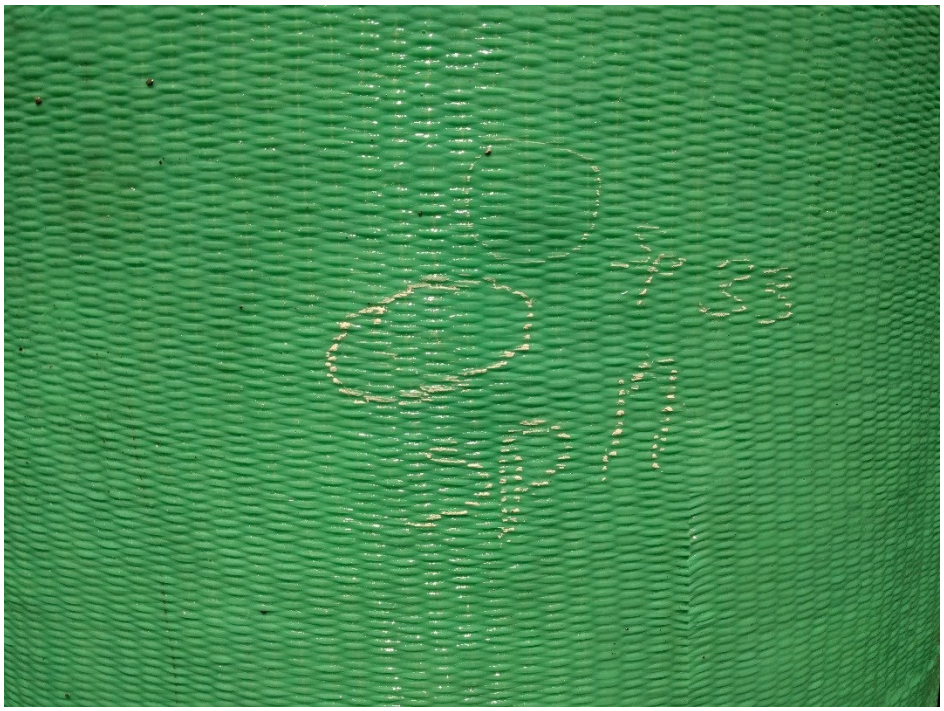

Figure 4.8: Elevated tap hammer readings on the east column of pier 3.

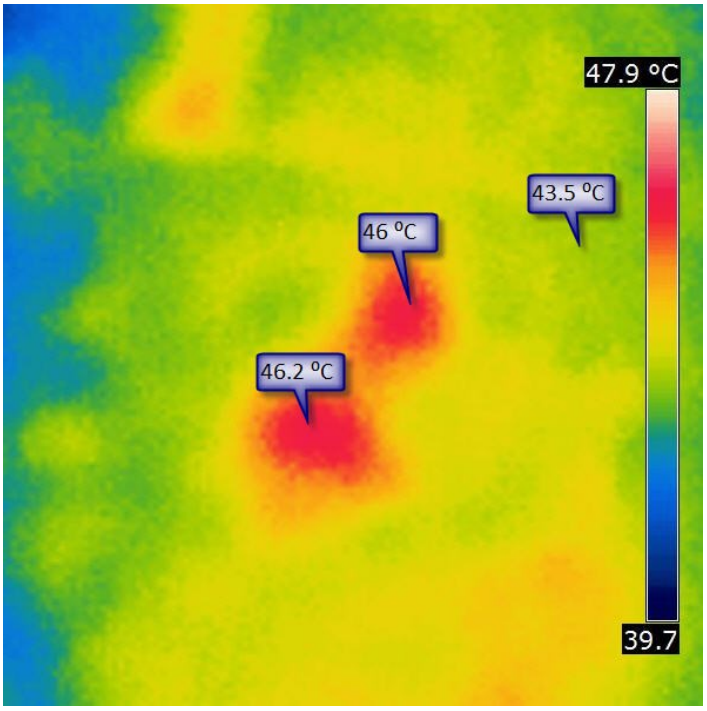

Figure 4.9: Infrared images associated with Figure 4.8.

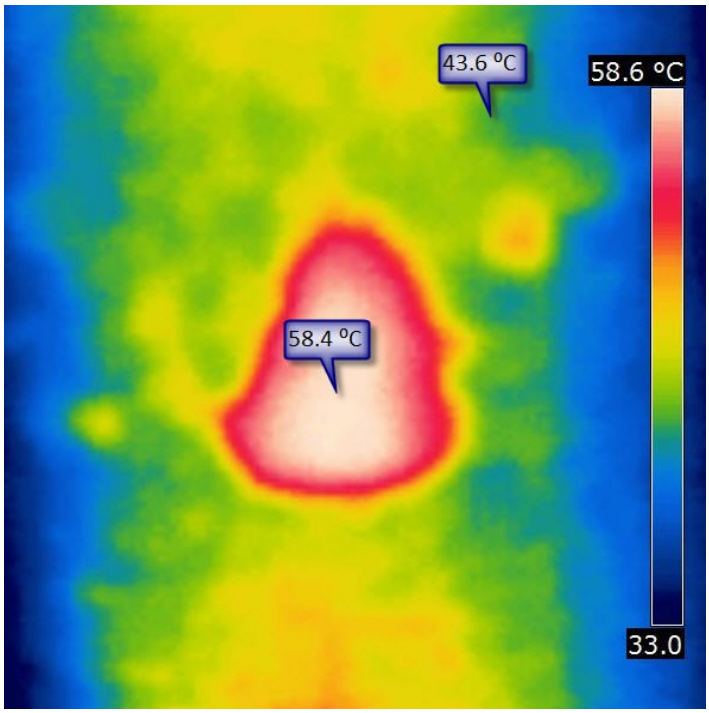

Figure 4.10: Infrared image of region 17 in Figure 4.7.

Figure 4.11: Area 13 on the center column of pier 3.

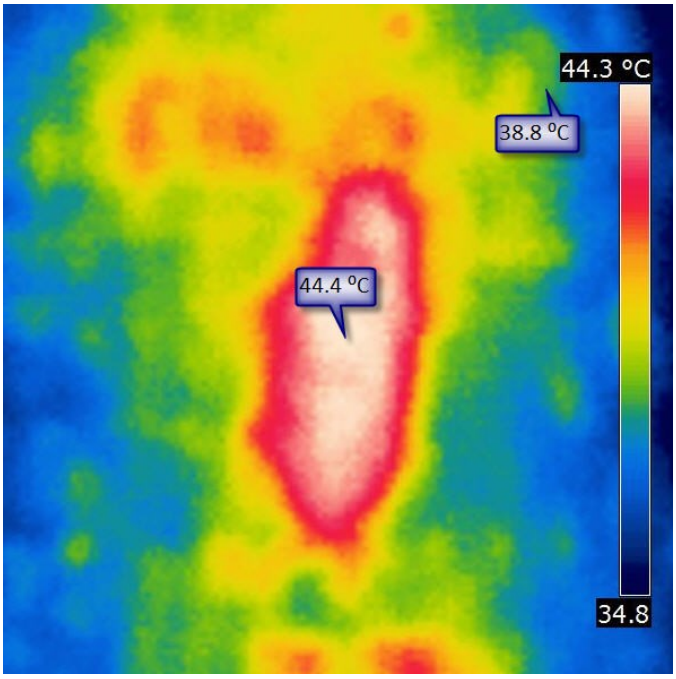

Figure 4.12: Area 13 debond.

Figure 4.13: Digital tap hammer region 12 on west column of pier 3.

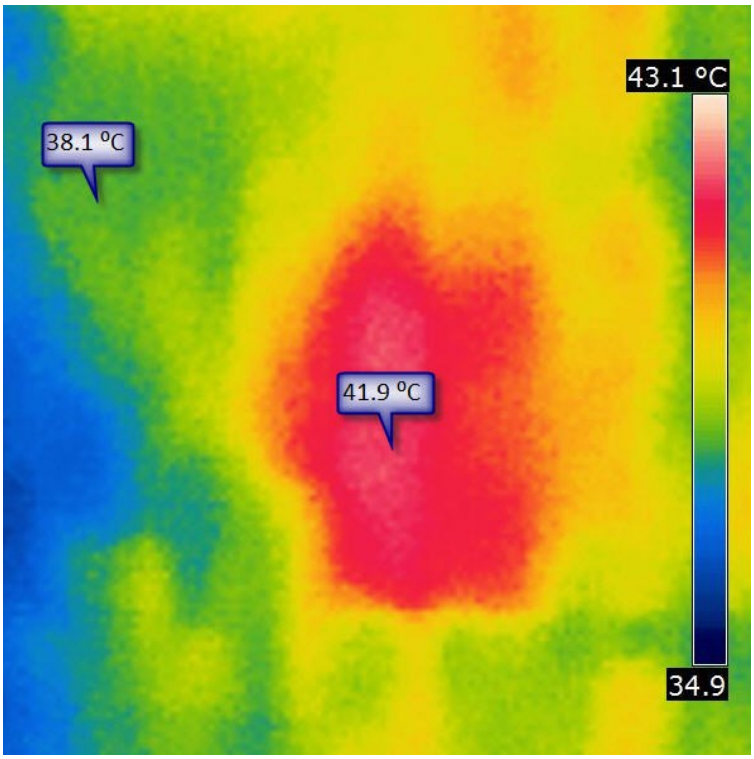

Figure 4.14: Denotes the infrared image for Figure 4.13.

Figure 4.15: Regions 7 and 8 of center column in pier 3.

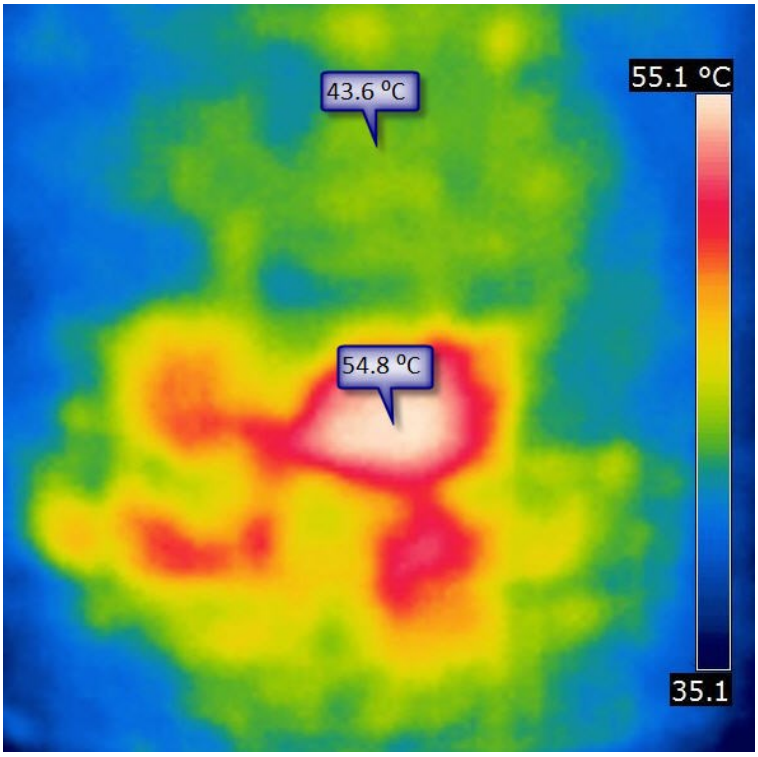

Figure 4.16: Infrared image correlating to region 7 in Figure 4.15.

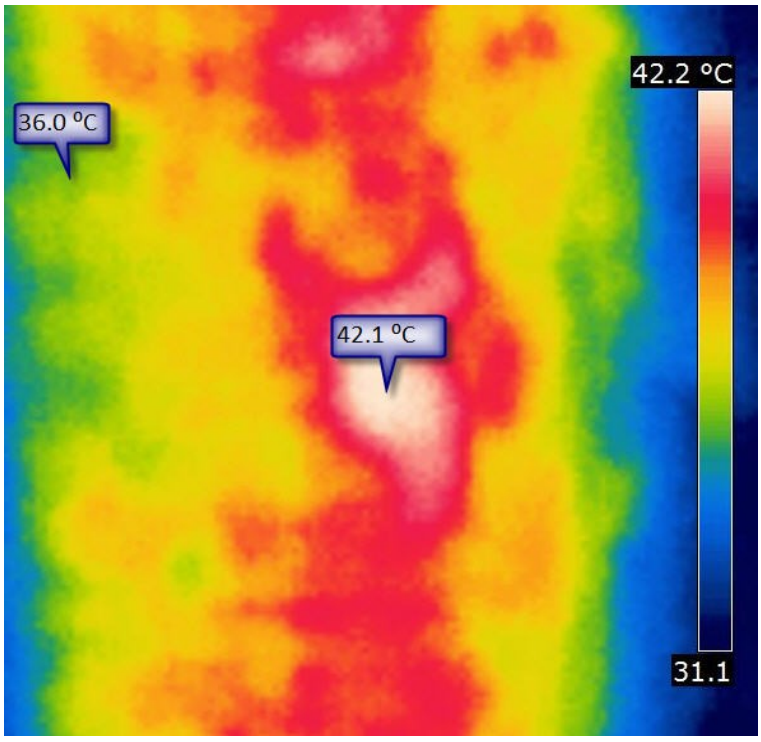

Figure 4.17: Infrared image for region 8 in Figure 4.15

4.4 PIERS 1 and 2 FIELD TESTING (JULY 26, 2017)

Testing on piers 1 and 2 were limited to tap hammer testing only due to a lack of electrical power and time constraints when working on pier 2. Testing on pier 2 was executed under night operations due to traffic polices set by the West Virginia Turnpike Authority. Digital tap hammer tests were conducted similar to those on pier 3, however, for both piers 1 and 2 a hydraulic man lift was used to inspect the upper portions of the columns. This meant that columns in piers 1 and 2 received a more thorough inspection near the pier cap than columns in pier 3. Testing of columns within pier 1 yielded results similar to pier 3 columns which was expected. Figure 4.18 illustrates some of the debond regions discovered in the wraps of pier 1. Columns within pier 2 however, produced high numbers of debonds. These columns were also shorter than the columns in piers 1 and 3 because they sit on top of the parapet wall. The number of debonds ranged from 60 to 82 per column. A breakdown of debonds per column and their respective digital tap hammer readings can be found in Appendix A.

Figure 4.18: Debonds found in the west column of pier 1.

After speaking with the inspector for the WVDOH about the high number of debonds, it was noted that the temperatures were much cooler when the contractor wrapped the columns of pier 2 than when the other columns of piers 1 and 3 were wrapped. The majority of the defects were found in the bottom half of the columns on pier 2. Some of the tap hammer results eluded to the fact that the defects were actually in the concrete and not within the wraps. These two phenomena are reinforced by the fact that the lower portions of columns in pier 2 underwent extensive concrete repairs as depicted in Figures 4.19, 4.20, 4.21. Examples of debonds that were found in the columns of pier 2 are shown in Figures 4.22 and 4.23.

Figure 4.19: Image showing all three columns of pier 2 and the necessary concrete repairs being made.

Figure 4.20: Center column of pier 2 in the process of being prepped for concrete repairs.

Figure 4.21: West column of pier 2 while corrosion inhibitors were being placed on the rebar.

Figure 4.22: An example of the amount of debonds found while testing columns pier 2.

Figure 4.23: The lower half of the west column on pier 2 and debonds that were found.

4.5 CONCLUSIONS FROM DIGITAL TAP HAMMER AND INFRARED TESTING

The overall intent of this project was to make the necessary repairs to the concrete columns and reinforcing bar, and to create a protective overlay that would prevent deterioration in the future. Thus, the concrete columns would be covered by the GFRP wrap. In this particular application, the GFRP acts as a protective shield and is nonstructural. The American Concrete Institute (ACI) has developed a guide (ACI 440.2R-17) related to the design and construction of FRP when externally bonded to concrete substrates. For the FRP wraps associated with this project, section 7.2.3 of Chapter 7 of ACI 440.2R-17 acts as the governing specifications for the evaluation and acceptance of the GFRP wraps. Section 7.2.3 applies to wraps used in structural application, and thus, this project is only concerned with two aspects of the section. ACI 440.2R-

17 indicates that, "small delaminations less than 2 in^2 each (1300 mm^2) are permissible as long as the delaminated area is less than 5% of the total laminate area and there are no more than 10 such delaminations per 10 ft^2 (I m^2)." Furthermore, ACI 440.2R-17 says that "large delaminations, greater than 25 $in.^2$ (16,000 mm^2), can affect the performance of the installed FRP and should be repaired by selectively cutting away the affected sheet and applying an overlapping sheet patch of equivalent plies; and delaminations less than 25 $in.^2$ (16,000 mm^2) may be repaired by resin injection or ply replacement, depending on the size and number of delaminations and their locations."

Based on the results from field observation and specifications from ACI440.2R-17, all of the debonds found via tap hammer and infrared testing could be filled with resin by the contractor. This is because the wrap is nonstructural. If the wrap was being used in a structural manner, then all of the delaminations greater than 25 in^2 would need to be removed and replaced. In Piers 1 and 3, the highest number of defects found in one column was 41 as shown in Appendix A. Columns within Piers 1 and 3 were roughly 377 ft^2 in total surface area. This means that the 41 debonds were scattered across 377 ft^2 equating to a little more than one debond in 10 ft^2 which is less than the 10 allowed by ACI. Although columns in Pier 2 produced the highest number of debonds per column with 82, the total area of each column in this pier was approximately 245 ft^2, which translated to a little more than 3 debonds per 10 ft^2. Again, this number falls in the permissible range of ACI 440.2R-17. It is also important to note that care should be given when patching the concrete structure at or below finish grade to achieve a smooth finish before applying the FRP wraps. There were multiple locations identified during tap hammer testing in piers 1 and 3 where the concrete at or below grade had considerable defects.

Delaminations or debonds are a concern for several reasons. FRP wraps are like other materials in that they are susceptible to freeze-thaw cycles. If for instance a debond was to go undetected, and remain a part of the structure, there is the possibility for water to enter the debond and remain for a period of time. In colder climates, water trapped in a debond can undergo a freeze-thaw cycle that would expand the debond in size, thus creating more issues for the FRP wrap. In addition to the freeze thaw cycles, the presence of debonds can ultimately reduce the strength of the wraps. Research published by Halabe et al. (2013) showed that a 5% debonded area produced

nearly a 20 to 30% reduction in the confined compressive strength of concrete cylindrical specimens. Further contributions of the research suggested that the ACI 440.2R code should reduce the permissible amount of debonds to less than 1.5 to 2% which resulted in roughly a 10% reduction in confined compressive strength.

Future considerations for projects of this nature would include better monitoring of the ambient temperature. If the wraps used in the project were structural, then the majority of the GFRP applied to the columns within pier 2 would have to be removed then replaced. Contractors working with the wraps must pay close attention during the application process (especially during nighttime operations) if temperatures begin to drop. The supplier or manufacturer of the FRP and resin products should provide information on the working temperatures for such rehabilitation projects.

5. CONCLUSIONS AND RECOMMENDATIONS

5.1 Conclusions

In the beginning of this report, a literature review was presented that focused on the development and implementation of nondestructive testing techniques including: digital tap hammer analysis and infrared thermography for applications in evaluating reinforced concrete structures and FRP composite bonded structures. The literature review also examined how different types of FRP are being utilized in bridge rehabilitation projects. The following conclusions can be made from this literature review.

- The digital tap hammer technology has evolved tremendously from the first rapid damage detection device (RD^3) created by Boeing and the Woodpecker WP-632, to finally the implementation of tap hammer analysis with unmanned aircraft systems (drones). All of which has increased the cost effectiveness and ease at which composite structures are tested and evaluated.

- Infrared Thermography is an efficient defect detection method for defects located near to the surface, but has limitations in identifying defects located deeper in the structures due to the phenomenon of lateral diffusion. When coupled with the digital tap hammer detection technique, IRT and be a valuable tool to verify the location of defects not only in concrete structures as shown in Clark et al. 2003 but also in other specimens such as Perspex and aluminum as in Gryzagoridis et al. 2016.

- In some cases, water filled debonds can be detected as “hot spots” via infrared thermography if the FRP layers or laminate above the defect is thin enough to allow the heat from the heat source to be absorbed by the water due to waters high specific heat value. Normally, debonds containing water would not show up as hot spots because water conducts heat faster than defect-free regions. If this were the case, the surface temperature above the water-filled debonds would be lower than the regions above the defect-free areas.

- The application of the FRP composite products in the area of bridge rehabilitation has become more widespread throughout the last 20 years. In most cases, rehabilitation involving FRP is more cost efficient and faster than conventional repair techniques. In some of the cases studied in this report, CFRP composites were able to enhance either the shear or flexural strength by some percentage while in other cases, the bending and shear stresses were reduced. GFRP plates have also been shown to increase flexural strength and reduce cracking on reinforced concrete beams (Saadatmanesh et al. 1991). In all but one instance, traffic across the bridges were either not affected or minimally reduced to one lane. The only exception was a pedestrian bridge in Canada where the design dedicated the rehabilitation process. When combining the success of the strengthening abilities with the ease of installation, FRP products have demonstrated how successful they can be in practical applications.
- With respect to bridge rehabilitation involving concrete repairs, it is crucial to act as soon as possible after noticing concrete degradation. In the case of the Turnpike Bridge, original designs for the rehab occur two years prior to construction. Thus, extensive concrete repairs were required to restore the columns to a suitable condition for wrapping of FRP.
- Special considerations must also be given when applying FRP products in cooler temperatures. The workability of the FRP will decrease in cooler temperatures in addition to prolonged curing times for the primers and resins. If temperatures start to cool down after the wrapping process has begun, then the overall integrity of the wrap may be compromised and subject to repairs after the wrap cures.
- In the early stages of the design of an FRP system, the engineer must decide if the system will serve as a structural or non-structural system. This classification is vital to how the FRP system will be designed, rehabilitated, tested, and evaluated. ACI 440.2R-17 has imposed different tolerances with respect to the evaluation and acceptance of the system depending on its classification.

- The results of this problem report provided several contributions to WVDOH and contractors looking to perform FRP composite field rehabilitations. Findings of this report contributed to the overall quality and success of the Turnpike Bridge rehabilitation by providing the contractor with information and insight about where potential debonds are located, and the appropriate corrective actions needed to be taken to ensure a quality wrap is produced. Furthermore, this report demonstrated to not only the contractor, but also the WVDOH, how easy and effective nondestructive testing techniques can be at evaluating FRP composites in the field after installation. This in turn has increased the confidence of the WVDOH in using FRP composites in bridge rehabilitation, and has led them to rehabilitate and evaluate additional bridges across the State using similar techniques as described in this project.

5.2 RECOMMENDATIONS FOR FIELD APPLICATION AND TESTING

In regards to the overall success of applying a FRP system in situ, achieving a strong bond between the FRP system and the substrate to which the FRP is being applied is imperative to the overall success of the system. New means and methods of applying FRP wraps to substrates have been developed, which involve the process of vacuum infused resin. While this new concept has been applied to bridge rehabilitation, it has not been done extensively. Testing has shown that this process creates a near seamless bond between the substrate and the FRP system. Debonds such as those described in Chapter 4 that are created due to the hand applied wet lay-up technique would essentially be eliminated. Currently, the costs associated with repairing delaminations either by removal and replacement or resin injection are relatively high. Implementing the vacuum infusion process would reduce labor costs associated with repairing FRP wraps after installation, and would in turn offset the initial costs of setting up the infusion process. Infrastructure applications involving vacuum infused resin techniques have been conducted in tunnel reinforcement, wind turbine blades, and other reinforcement projects (Summerscales et al. 2004).

Special consideration should be given to the area of concrete repairs prior to applying the wraps. Ensuring that the surface of the concrete is smooth and free of sharp edges or holes is vital for the overall success of the rehabilitation process. Care given to the formwork used to reconstruct

the geometric shape of the structure in the early stages of rehabilitation would pay dividends in time saved during FRP application, evaluation, and repairs if needed. Contractors executing the field portion of the rehabilitation should explore a variety of repair mortars or grouts as well as different forming techniques to limit the costs related to surface preparation prior to wrapping the structure with FRP. In some cases, composite structures similar to sonotubes have been used as a form, and because the form itself was an FRP, the final FRP wraps were installed directly on top of the form.

In terms of field testing and evaluation of FRP systems, alternative heating techniques should be explored to alleviate certain heating problems related to the accessibility of the test areas and the lack of uniformity in heating. When conducting in situ evaluations, a combination of at least two nondestructive testing techniques should be utilized as opposed to using a single technique. The combination of IRT and digital tap testing techniques worked well for FRP system studied in this report. The digital tap testing device offered a quick "world atlas" of the debonds across the entire column while the IRT served as more detailed "road map" and check on the tap hammer results. The combined efforts of the two techniques predicted debond locations that correlated well with one another most of the time.

REFERENCES

1. ACI 440.2R-17 (2017). "Guide for the Design and Construction of Externally Bonded FRP Systems for Strengthening Concrete Structures." *American Concrete Institute*, Farmington Hills, MI, 20.
2. Association of American Railroads (AAR): "A Short History of U.S. Freight Railroads." AAR, Washington (2014)
3. ASTM D3039 (2017). "Standard Test Method for Tensile Properties of Polymer Matrix Composite Materials." American International, West Conshohocken, PA.
4. Avdelidis, N. P., Gan, T., Ibarra-Castanedo, C., & Maldague, X. P. (2011). "Infrared Thermography as a Nondestructive Tool for Materials Characterisation and Assessment." *Thermosense: Thermal Infrared Applications XXXIII*. doi:10.1117/12.887403
5. Bridges. (2017). Retrieved from https://www.infrastructurereportcard.org/cat-item/bridges/
6. Choi, Y. S., Yi, S., Kim, M. Y., Jung, W. Y., & Yang, E. I. (2014). "Effect of Corrosion Method of the Reinforcing Bar on Bond Characteristics in Reinforced Concrete Specimens." *Construction and Building Materials, 54*, 180-189. doi:10.1016/j.conbuildmat.2013.12.065
7. Clark, M., Mccann, D., & Forde, M. (2003). "Application of Infrared Thermography to the Non-Destructive Testing of Concrete and Masonry Bridges." *NDT & E International,36*(4), 265-275. doi:10.1016/s0963-8695(02)00060-9
8. Cromwell, J., Harries, K., & Shahrooz, B. (2011). "Environmental Durability of Externally Bonded FRP Materials Intended for Repair of Concrete Structures." *Construction and Building Materials, 25*(5), 2528-2539. doi:10.1016/j.conbuildmat.2010.11.096
9. GangaRao, H. V. S., Halabe, U. B., Liang, R., Skidmore, M., Kotha, M., and Perisetty, N. K. (2015), "FRP Wrap of the Madison Avenue Bridge," Final Report No. RP 268, submitted to the West Virginia Department of Transportation – Division of Highways, Charleston, WV, August, 1-49.

10. Georgeson, G. E., Lea, S., & Hansen, J. (1996). "Electronic Tap Hammer for Composite Damage Assessment." *Nondestructive Evaluation of Aging Aircraft, Airports, and Aerospace Hardware (SPIE)*. doi:10.1117/12.259107
11. Gryzagoridis, J. and Findeis, D. (2016). "Tap Testing vs. Thermography." *The e-Journal of Nondestructive Testing*, 21(7).
12. Halabe, U. B., Dutta, S. S., & GangaRao, H. V. (2013). "Behavior of FRP Composite Wrapped Concrete Cylinders with Embedded Debonds." *Structures Congress 2013*. doi:10.1061/9780784412848.050
13. Halabe, U., Dutta, S. and GangaRao, H. (2008). "NDE of FRP Wrapped Columns Using Infrared Thermography." *Review of Quantitative Nondestructive Evaluation*, American Institute of Physics. 27 (CP975), 1387-1394. Available online at: http://aip.scitation.org/doi/abs/10.1063/1.2902597 [Accessed 31 Aug. 2017].
14. Halabe, U., Kotha, M. and Hota, G. (2014). "Condition Assessment of Reinforced Concrete and FRP Composite Structural Components using NDT Techniques." *The American Society for Nondestructive Testing*, August, 169-176.
15. Heida, J.H.; Derk, J.P. "Evaluation of Non-Destructive Inspection Methods for Composite Aerospace Structures." *NDT Prog.*, *2011*, 1–12.
16. Huston, D., Cui, J., Burns, D., Hurley, D. (2011). "Concrete Bridge Deck Condition Assessment with Automated Multisensor Techniques." Struct. Infrastruct. Eng. **7**(7–8), 613–623.
17. Hutchinson R.L., Rizkalla, S.H. (1999). "Shear Strengthening of AASHTO Bridge Girders Using Carbon Fibre Reinforced Polymer Sheets." *Proceedings of the Fourth International Symposium on Fibre Reinforced Polymer Reinforcement for Reinforcement Concrete Structures*. ACI Publications SP-188, 945 –56.
18. Hutchinson, R., Tadros, G., Kroman, J., Rizkalla, S. (2003). "Use of Externally Bonded FRP Systems for Rehabilitation of bridges in Western Canada." in Rizkalla, S.; Nanni, A. (Eds.). *Field Applications of FRP Reinforcement: Case Studies ACI SP-215*. ACI, Farmington Hills, 239–248.

19. Klaiber, F.W., Dunker, K. F., Wipf, T.J., and Sanders, W.W., Jr. (1987). "Methods of Strengthening Existing Highway Bridges." Report No. 293, National Cooperative Highway Research Program (NCHRP).
20. Kotha, M. (2013). *Nondestructive Evaluation of Concrete and Composite Bridges Using Infrared Thermography and Ground Penetrating Radar*, Master's Problem Report, West Virginia University, Morgantown, WV.
21. Moreu, F., Ayorinde, E., Mason, J., Farrar, C., & Mascarenas, D. (2017). "Remote Railroad Bridge Structural Tap Testing Using Aerial Robots." *International Journal of Intelligent Robotics and Applications*. doi:10.1007/s41315-017-0041-7
22. (n.d.). Retrieved August 31, 2017, from https://www.nde-ed.org/AboutNDT/aboutndt.htm
23. Liang, R., and GangaRao, H. (2013). "Fiber-Reinforced Polymer Composites in Environmental Engineering Applications." in *Developments in Fiber-Reinforced Polymer (FRP) Composites for Civil Engineering*, edited by N. Uddin, Woodhead Publishing, Cambridge, UK (2013).
24. Saadatmanesh, H., & Ehsani, M.R. (1991). "RC Beams Strengthened with GFRP Plates. I: Experimental Study." *Journal of Structural Engineering, 117*(11), 3417-3433. doi:10.1061/(asce)0733-9445(1991)117:11(3417)
25. Stallings, J.M., Tedesco, J.W., El-Mihilmy, M., & Mccauley, M. (2000). "Field Performance of FRP Bridge Repairs." *Journal of Bridge Engineering, 5*(2), 107-113. doi:10.1061/(asce)1084-0702(2000)5:2(107)
26. Summerscales, J., & Searle, T.J. (2005). "Low-Pressure (Vacuum Infusion) Techniques for Moulding Large Composite Structures." *Proceedings of the Institution of Mechanical Engineers, Part L: Journal of Materials: Design and Applications, 219*(1), 45-58. doi:10.1243/146442005x10238
27. Valluzzi, M.R., Grinzato, E., Pellegrino, C., & Modena, C. (2008). "IR Thermography for Interface Analysis of FRP Laminates Externally Bonded to RC Beams." *Materials and Structures, 42*(1), 25-34. doi:10.1617/s11527-008-9364-z

APPENDIX A

Pier 1		
East Column		
Good Range 1110 – 1204 μs		
Area	**Tap Hammer Readings (μs)**	**Debond Size (in)**
1	1235 - 1858	3.5 x 5.25
2	1340 - 4666	4.5 x 4.5
3	1215 - 1297	4.5 x 6
4	1235 - 1321	4.5 x 5
5	1419 - 2021	3.25 x 3.5
6	1230 - 2190	6.5 x 10
7	1299 - 1738	3 x 5
8	1401 - 2479	8 x 4
9	1244 - 1790	4.75 x 8
10	1262 - 1421	1.5 x 3.5
11	1235 - 1654	2 x 5
12	1313 - 1702	2 x 5
13	1336 - 1809	2.25 x 4
14	1253 - 1611	3.5 x 3
15	1537 - 2307	3.5 x 4
16	1355 - 1609	2.5 x 10
17	1237 - 1502	8.5 x 9
18	1340 - 2405	4.25 x 3.75
19	1357 - 2513	4.5 x 6.5
20	1399 - 1790	4 x 4
Seam	1342 - 1510	1.5 x 11.5
21	1565 - 2045	3.75 x 5.5
22	1234 - 1672	2.25 x 4
23	2194 - 2866	6 x 3.75
24	1246 - 1992	6.5 x 4
25	1240 - 1506	2 x 2
26	1324 - 1574	1.5 x 3.5
27	1307 - 1538	8 x 5
28	1260 - 2061	2.75 x 4.5
29	1420 - 2220	2.5 x 4
30	1219 - 1335	4 x 5
31	1292 - 2106	3 x 6.5

32	1211 - 1304	3 x 5.5
33	1302 - 2184	2.5 x 4
34	1229 - 1651	2 x 3
35	1618 - 1207	2.5 x 2.5
36	2181 - 2911	7 x 4
37	1275 - 2377	4.5 x 3
38	1240 - 1948	4 x 3
39	1289 - 3389	7.5 x 16.5
40	1239 - 1942	4 x 5

Pier 1		
Center Column		
Good Range 1071 – 1204 μs		
Area	**Tap Hammer Readings (μs)**	**Debond Size (in)**
1	1215 - 1595	2.25 x 2.5
2	1262 - 1691	16.5 x 5
3	1273 - 1640	2 x 6
4	1218 - 1459	2.5 x 5
5	1213 - 1342	2 x 4
6	1244 - 1727	9.5 x 5
7	1301 - 1795	3.5 x 3.5
8	1340 - 2645	3 x 8
9	1294 -1756	5.5 x 6
10	1270 - 1392	5.5 x 5
11	1310 - 2280	5.5 x 5.5
12	1308 - 1667	3 x 3
13	1340 - 2997	3 x 5.5
14	1270 - 1737	2.5 x 3.5
15	1278 - 1661	3.5 x 2
16	1265 - 1396	4 x 3
17	1252 - 1449	3.25 x 4.5
18	1284 - 1790	2.5 x 4
19	1224 - 1927	3 x 4
20	1256 - 1449	2.75 x 8.75
21	1404 - 1829	2.5 x 3
22	1351 - 1603	1.75 x 4.75

23	1276 - 1803	6 x 5
24	1306 - 1551	2 x 2.5
25	1301 - 1454	4 x 4.75
26	1268 - 1940	2 x 3.75
27	1303 - 2372	3 x 7
28	1255 - 1440	2.75 x 3.5
29	1261 - 1299	5.25 x 8.75
30	1243 - 1457	2 x 3
31	1297 - 1519	5.5 x 10.5
32	1306 - 1717	2.5 x 3.5
33	1353 - 1559	3.75 x 4
34	1379 - 1878	6 x 11
35	1314 - 1369	2.5 x 5
36	1316 - 2014	5 x 7
37	1250 - 1651	2.5 x 4
38	1263 - 1560	7 x 10

Pier 1		
West Column		
Good Range 1050 – 1210 μs		
Area	**Tap Hammer Readings (μs)**	**Debond Size (in)**
1	1399 - 2454	3.5 x 6
2	1275 - 2013	3.5 x 8
3	1286 - 1396	3 x 5
4	1285 - 1607	9.5 x 3
5	1267 -2864	3 x 7
6	1244 - 1735	5 x 6
7	1285 - 2063	2.5 x 2.75
8	1295 - 1446	3 x 2.75
9	1395 - 1848	2.5 x 2
10	1309 - 1448	5 x 3
11	1307 - 1672	5.5 x 7
12	1281 - 1497	2 x 3.5
13	1298 - 1561	2 x 2
14	1369 - 1657	4 x 2.5
15	1277 - 1343	2 x 3

16	1272 - 1862	3.25 x 10
17	1357 - 1568	3.25 x 5.5
18	1278 - 1416	2.25 x 2.5
19	1275 - 1382	3 x 3.75
20	1347 - 2327	11 x 17.5
21	1259 - 1667	4 x 7
22	1252 - 1317	4.5 x 5
23	1272 - 1618	4 x 4
24	1262 - 1369	5 x 7
25	1268 - 1851	3 x 9
26	1237 - 2116	9 x 5
27	1233 - 1370	5 x 4
28	1236 - 1610	4 x 16
29	1234 - 1479	5 x 2.5
30	1222 - 1267	3.5 x 5
31	1290 - 1313	6.5 x 2.5
32	1267 - 1442	4 x 2
33	1241 - 1252	3.25 x 2.5
34	1268 - 1485	3.5 x 2.5
A	1243 - 1654	14.5 x 16

Pier 2		
East Column		
Good Range 1081 – 1205 μs		
Area	**Tap Hammer Readings (μs)**	**Debond Size (in)**
1	1294 - 1517	2 x 2
2	1240 - 1711	4.25 x 4.5
3	1240 - 1889	3 x 6
4	1317 - 1732	3.5 x 11
5	1283 - 1391	3 x 13
6	1221 - 1470	4.25 x 2.75
7	1366 - 1920	5 x 2.5
8	1349 - 1722	4 x 2
9	1224 - 1298	4 x 3
10	1210 - 1284	3 x 4
11	1264 - 1309	3.5 x 3

12	1490 - 1871	4.5 - 3
13	1446 - 1767	2.5 x 3.5
14	1240 - 1366	3 x 8
15	1219 - 1447	2 x 3.25
16	1250 - 1494	4 x 5.75
17	1248 - 1840	2 x 3
18	1222 - 1396	3 x 4
19	1244 - 2043	8 x 3
20	1228 - 1330	4.75 - 4.5
21	1217 - 1302	10.5 x 3
22	1248 - 1348	4.5 x 5
23	1205 - 1423	4 x 11
24	1220 - 1581	2.5 x 11
25	1337 - 1881	4 x 2.5
26	1337 - 2249	6 x 5
27	1298 - 1404	5.5 x 6
28	1230 - 1335	2 x 3
29	1219 - 1260	3 x 4
30	1283 - 1344	4.5 x 3
31	1272 - 1876	4 x 6.5
32	1208 - 1680	12 x 3.5
33	1827 - 2590	1.5 x 3
34	1252 - 1304	2.25 x 3
35	1291 - 1344	3.5 x 1.5
36	1237 - 1357	3.5 x 1.5
37	1302 - 1508	9.5 x 14.5
38	1267 - 1359	3 x 3.25
39	1243 - 1422	11 x 6
40	1330 - 1742	2.5 x 12
41	1213 - 1338	2 x 3
42	1286 - 1421	11 x 6.5
43	1210 - 1420	4.5 x 5
44	1305 - 1904	7 x 3.5
45	1418 - 1636	5 x 3
46	1319 - 1795	4.5 x 3.5
47	1320 - 1659	3 x 5
48	1203 - 1925	7 x 2.5
49	1257 - 2058	2.5 x 7
50	1204 - 1809	17 x 5

51	1247 - 1389	2 x 4
52	1219 - 2281	9.5 x 4.5
53	1250 - 1300	3.5 x 4.5
54	1220 - 1404	2.5 x 1.75
55	1222 - 1364	13 x 6.5
56	1285 - 1896	3.75 x 5
57	1243 - 1746	4 x 2
58	1300 - 2371	6 x 4
59	1883 - 2764	3.5 x 5
60	1271 - 2826	10 x 5

Pier 2		
Center Column		
Good Range 1100 – 1208 μs		
Area	**Tap Hammer Readings (μs)**	**Debond Size (in)**
1	1238 - 1630	9 x 3.5
2	1213 - 2008	9 x 4.5
3	1225 - 1380	7 x 3
4	1222 - 1994	2 x 2
5	1225 - 1258	1.5 x 3
6	1225 - 1737	4 x 6
7	1306 -1707	6 x 3
8	1220 - 1667	8 x 3
9	1230 - 1498	5.5 x 3
10	1242 - 1818	5 x 3
11	1296 - 1340	7.5 x 2.5
12	1216 - 1266	4.5 x 2
13	1230 - 1901	3.5 x 3
14	1214 -1278	6.25 x 2
15	1282 - 1339	3.5 x 5
16	1222 - 1390	12 x 9
17	1243 -1463	2 x 2
18	1267 - 1463	2 x 2
19	1262 -1463	2.5 x 2.5
20	1231 - 1582	2.5 x 3
21	1299 - 1528	2.25 x 2.75
22	1242 - 1903	7.5 x 6.5
23	1233 - 1661	11 x 3.5
24	1218 -1265	4 x 2.75
25	1287 - 1578	7 x 2.75
26	1220 -1287	2 x 8
27	1228 -1427	2 x 2
28	1250 - 1485	4.5 x 3.5
29	1302 - 1688	3 x 1.5
30	1244 - 1350	6 x 9
31	1234 - 1584	3 x 2.75
32	1262 - 1671	2 x 4
33	1329 - 2165	3.5 x 3
34	1222 - 1276	2 x 4

35	1207 -1472	3 x 2.25
36	1209 - 1229	2.25 x 2
37	1220 - 1681	11 x 4.5
38	1319 - 1808	12 x 3.25
39	1220 - 1681	6 x 3
40	1251 - 2658	8 x 4
41	1377 - 1975	5.5 x 2.5
42	1216 - 1301	8.25 x 3
43	1281 - 1802	7 x 3
44	1246 - 1646	7.75 x 4.25
45	1242 - 1724	6.5 x 4
46	1267 - 2080	10 x 3
47	1285 - 1622	6 x 2
48	1384 - 1690	2.5 x 6.5
49	1222 - 1403	5.5 x 2.5
50	1498 - 1995	5.5 x 2.5
51	1261 - 1580	6 x 11
52	1281 - 1362	2 x 3.5
53	1225 - 1291	5 x 2
54	1226 -2411	8.5 x 4
55	1226 - 1401	2 x 4
56	1219 - 1469	4 x 6.5
57	1223 - 1380	19 x 2.5
58	1259 - 2207	2.75 x 6
59	1257 - 1411	3 x 2
60	1257 - 1335	2 x 6
61	1222 -2337	2.5 x 7
62	1419 - 1904	9.5 x 3
63	1302 - 1848	5.5 x 3.25
64	1430 - 1680	2.5 x 10
65	1323 - 1840	6 x 3
66	1235 - 1786	3 x 4
67	1529 - 1725	2.5 x 4
68	1306 -1611	2.5 x 1.5
69	1677 - 2479	7.25 x 3
70	1250 - 1348	3 x 2
71	1249 - 1413	8 x 8
72	1291 - 2143	13.5 x 3
73	1304 - 1692	3.5 x 5.5

74	1317 - 1902	6.5 x 3
75	1412 - 1801	5.75 x 2.25
76	1226 - 1259	2.25 x 4
77	1511 - 2060	3.25 x 11
78	1226 - 1396	4 x 3
79	1384 - 1600	2 x 2.5
80	1357 - 1491	1.5 x 2
81	1222 - 1230	8 x 1.75
82	1378 - 1494	2 x 6

Pier 2		
West Column		
Good Range 1096 – 1205 μs		
Area	**Tap Hammer Readings (μs)**	**Debond Size (in)**
1	1260 - 2064	9.5 x 4
2	1337 - 1668	2.25 x 2.5
3	1233 - 1547	3 x 4.25
4	1309 - 2165	2.5 x 7
5	1404 - 1889	8 x 2.5
6	1386 - 1710	4 x 2
7	1234 - 1407	4 x 6
8	1750 - 3457	3.5 x 2
9	1256 - 1502	1.5 x 5.5
10	1415 - 1601	2 x 2
11	1455 - 2296	6 x 3.25
12	1231 - 1364	4.5 x 2
13	1431 - 1676	5 x 3
14	1368 - 1640	4 x 2
15	1331 - 1832	8 x 4
16	1536 - 2050	4 x 5
17	1370 - 1674	1.5 x 2.5
18	1431 - 2489	9 x 5
19	1244 - 1569	1 x 3
20	1266 - 1331	5 x 3
21	1232 - 1594	12 x 3
22	1289 - 1353	6.25 x 3.5

23	1351 - 1597	4 x 2.5
24	1219 - 2000	11.5 x 1.5
25	1234 - 1393	3 x 4
26	1359 - 1505	4 x 3.5
27	1409 - 2197	3 x 5
28	1235 - 1911	2 x 3.5
29	1296 - 1602	11 x 4.5
30	1307 - 1442	3 x 3.5
31	1235 - 1706	4 x 1.5
32	1213 - 1368	4.5 x 5.5
33	1226 - 1260	4 x 6.25
34	1248 - 1301	4.5 x 3
35	1232 - 1556	3 x 2
36	1273 - 1477	2.75 x 4.5
37	1617 - 2428	3 x 3.5
38	1264 - 1552	5.25 x 2
39	1368 - 2391	1.75 x 5
40	1310 - 1699	4 x 5
41	1215 - 1316	4 x 3
42	1267 - 1303	2 x 4.5
43	1296 - 1599	3 x 4
44	1555 - 1769	8 x 5.5
45	1352 - 2099	10 x 4
46	1661 - 2348	8 x 7
47	1534 - 1789	2 x 2.5
48	1590 - 1811	2 x 1.75
49	1218 - 1306	6 x 3
50	1252 - 1303	10 x 2.5
51	1283 - 1788	3 x 11
52	1214 - 1345	4 x 6.25
53	1213 - 1272	7.5 x 2
54	1420 - 1751	3.25 x 2.5
55	1304 - 1601	4.5 x 1.5
56	1518 - 2194	5 x 3
57	1249 - 1937	8.5 x 3
58	1275 - 1901	9 x 3.5
59	1215 - 1233	6 x 1.5
60	1221 - 1782	4 x 3
61	1229 - 1430	3 x 2.25

Pier 3		
East Column		
Good Range 1048 – 1199 μs		
Area	**Tap Hammer Readings (μs)**	**Debond Size (in)**
1	1202 - 1205	3 x 3
2	1315 - 1348	3.5 x 3
3	1258 - 1279	3 x 2.5
4	1235 - 1404	1.5 x 2
5	1304 - 1555	2 x 2
6	1199 - 1351	2 x 2
7	1248 - 1470	2.25 x 2.25
8	1196 - 1410	1 x 2
9	1256 - 1437	1 x 1
10	1893 - 2309	2.5 x 6
11	1309 - 1448	1.25 x 1.5
12	1329 - 1657	1.25 x 1.5
13	1228 - 1796	1 x 3.5
14	1305 - 1588	2 x 3.5
15	1204 - 1308	1.75 x 4.25
16	1200 - 1285	1.5 x 1.5
17	1202 - 1314	1.75 x 3.5
18	1219 - 1272	2.5 x 3
19	1226 - 2115	2 x 2
20	1232 - 1509	1.5 x 2
21	1227 - 1435	2 x 2.5
22	1290 - 1670	2 x 3.5
23	1260 - 1950	1 x 2
24	1413 - 1732	1.5 x 2.5
25	1212 - 1316	2 x 4
26	1210 - 1288	1.5 x 1.5
27	1216 - 1299	1.5 x 1.5
28	1667 - 2182	2.5 x 3
29	1372 - 1907	2.5 x 1.5
30	1209 - 1424	3 x 5
31	1208 - 1238	1.5 x 2.5
32	1226 - 1292	3 x 7

33	1206 - 1278	2 x 2
34	1210 - 1267	1.5 x 2.5

Pier 3		
Center Column		
Good Range 1053 – 1185 μs		
Area	**Tap Hammer Readings (μs)**	**Debond Size (in)**
1	1252 - 1552	2 x 3
2	1208 - 1257	1.5 x 3
3	1219 - 1432	1.5 x 2
4	1261 - 1600	1.5 x 3
5	1209 - 1395	2.5 x 12
6	1219 - 1479	1.75 x 2.5
7	1226 - 1422	5 x 3.5
8	1297 - 2591	3 x 4
9	1257 - 1280	2 x 3
10	1249 - 1556	1.5 x 3.5
11	1202 - 1236	1.5 x 2
12	1232 - 1236	2 x 3.5
13	1212 - 1365	2.5 x 5.5
14	1248 - 1473	1.5 x 2
15	1204 - 1385	1.5 x 2.5
16	1248 - 1369	3 x 1.5
17	1217 - 2420	5 x 5.5
18	1222 - 1529	2 x 1.5
19	1212 - 1353	2.5 x 5
20	1214 - 1331	1.5 x 2
21	1215 - 1360	3.5 x 4
22	1204 - 1232	2 x 2
23	1214 - 1232	2 x 2
24	1240 - 2089	5 x 2
25	1221 - 1439	1.5 x 1.5
26	1209 - 1236	3 x 4
27	1215 - 2129	2.5 x 2.25
28	1219 - 1438	2 x 2
29	1200 - 1375	1.5 x 4
30	1237 - 1894	4.5 x 1.5

31	1231 - 1520	2.5 x 3
32	1220 - 2351	3 x 4
33	1209 - 1258	1.5 x 2
34	1210 - 1300	1.25 x 2.5
35	1212 - 1284	1.25 x 1.5
36	2050 - 2521	3 x 4
37	1283 - 1584	3.5 x 7
38	1215 - 1537	2.5 x 4.5
39	1353 - 2005	2.5 x 4
40	1211 - 1290	2.25 x 3
41	1211 - 1240	1.5 x 3.75

Pier 3		
West Column		
Good Range 1020 – 1177 μs		
Area	**Tap Hammer Readings (μs)**	**Debond Size (in)**
1	1254 - 1417	3.5 x 4.5
2	1205 - 1354	3.25 x 3.5
3	1213 - 1490	9 x 7
4	1216 - 1325	1.5 x 2
5	1240 - 1310	2 x 3
6	1218 - 1292	2 x 4
7	1216 - 1317	2 x 3.5
8	1216 - 1261	2 x 2.5
9	1216 - 1721	3.5 x 5
10	1260 - 1645	3 x 5.5
11	1215 - 1372	4 x 10
12	1208 - 1258	5 x 4
13	1207 - 1387	5 x 4
14	1284 - 2106	1.5 x 5
15	1222 - 1504	12.5 x 4.5
16	1284 - 1333	1.75 x 4.5
17	1214 - 1252	2.5 x 3.75
18	1245 - 1426	4.5 x 5
19	1259 - 1479	3 x 7
20	1190 - 1274	1.25 x 2.5

21	1240 - 1390	1.5 x 1.5
22	1218 1356	6 x 2
23	1203 - 1294	1.75 x 2.75
24	1208 - 1333	1.5 x 3.5
25	1240 - 3440	7 x 6.5
26	1211 - 1971	2.5 x 3
27	1250 - 1389	1.5 x 3
28	1209 - 1854	7 x 7.5
29	1207 - 1355	2.25 x 4
30	1206 - 1575	4 x 7
31	1275 - 1770	1.75 x 2